Projet AGES
Appui à la Gestion des Eaux Souterraines
dans le Bassin du Niger

Mapping of surface water dynamics in the Niger Basin

A remote sensing approach using Landsat time series

Technical Report No 8

Hanover, 2020

Niger Basin Authority (NBA)

Bundesanstalt für Geowissenschaften und Rohstoffe

german cooperation
DEUTSCHE ZUSAMMENARBEIT

Authors: Matthias Heckmann

Commissioned by: Federal Ministry for Economic Cooperation and Development (Bundesministerium für wirtschaftliche Zusammenarbeit und Entwicklung, BMZ)
Project: Appui à la Gestion des Eaux Souterraines dans le Bassin du Niger (AGES)
BMZ-No.: 2019.2342.4
BGR-No.: 05-2411

Date: drafted 2017 (published 2020)

Contents

Figures

Tables

Abbreviations

AGES	Appui à la Gestion des Eaux Souterraines dans le Bassin du Niger
ABN	Autorité du Bassin du Niger
AWEI	Automated Water Extraction Index
BGR	Federal Institute for Geosciences and Natural Resources
BMZ	Federal Ministry for Technical Cooperation and Development
BRGM	Bureau de recherches géologiques et minières
CFmask	C Function of Mask (CFMask) algorithm
DCW	Digital Chart of the World
DEM	Digital Elevation Model
DLR	National aeronautics and space research centre of the Federal Republic of Germany
ENVISAT	Environmental Satellite
ETM+	Enhanced Thematic Mapper Plus
FAO	Food and Agriculture Organization of the United Nations
GIS	Geographic Information System
GIZ	Gesellschaft für Internationale Zusammenarbeit
GLWD	Global Lakes and Wetlands Database
HydroSHEDS	Hydrological data and maps based on SHuttle Elevation Derivatives at multiple Scales
IGN	Institute Géographique National (France)
LCCS	Land Cover Classification System
LGAC	Landsat Global Archive Consolidation
MERIS	Medium Resolution Imaging Spectrometer, satellite ENVISAT
MNDWI	Modified Normalized Difference Water Index
MODIS	Moderate Resolution Imaging Spectroradiometer, satellites Terra & Aqua
NBA	Niger Basin Authority
NDWI	Normalized Difference Water Index
NGA	National Geospatial-Intelligence Agency
NIMA	National Imagery and Mapping Agency
NIR	Near Infrared
OLI	Operational Land Imager
ONC	Operational Navigation Chart
RGB	Red-Green-Blue
SAR	Synthetic Aperture Radar
SLC	Scan Line Corrector
SRTM	Shuttle Radar Topographic Mission
SWDB	SRTM Water Body Data
SWIR	Shortwave infrared
TCW	Tasselled Cap Wetness Index
TM	Thematic Mapper
USGS	United States Geological Service
VIS	Visible light
VMap 0	Vector Smart Map Level 0
WRS-2	Worldwide Reference System 2
WWF	World Wildlife Found

1 Summary

Drawing on remote sensing techniques, this study analyses a **32-year time series** of **Landsat imagery** (1984-2016) for the boundary region of Benin, Niger, and Nigeria. A spectral index algorithm, the **Modified Normalized Difference Water Index** (MNDWI, Xu 2006), was applied to extract water bodies. Publicly available data, open source software, and reproducible analytical procedures allow transferring the approach to small-scale studies of surface water monitoring in the member states of the Niger Basin Authority. The time series analysis provides baseline information summarizing the surface water dynamics of the past three decades and estimating the **temporal and spatial variability of the average extent and duration of flooding**. The resulting maps present probability of flooding and surface water seasonality.

Probability of flooding reflects the frequency of flooding or the water recurrence interval. Calculated on an annual and a monthly basis it differentiates between three flooding classes:

- areas reliably flooded every year/month,
- areas frequently flooded at least once in ten years, and
- areas rarely flooded (less than once in 10 years).

Surface water seasonality describes the average annual duration of flooding. **Permanent water bodies** delineate areas flooded on average twelve months a year.

Used as a flood hazard map, peak flood extents up to a 10-year recurrence interval are delineated and provide information for risk management and disaster prevention. Urban development and infrastructure planning can fall back on the maps to minimize **flood vulnerability.** The probability of flooding and the water seasonality maps will facilitate the appraisal of the amount and relevance of indirect **groundwater recharge** via seasonal ponds.

Shortcomings are the low number of valid observations per year/month and the poor discriminatory power of the spectral index, which in particular limit the interpretation of rarely flooded areas with a probability of flooding less than 10 % (flooded less than once in 10 years) but also areas with a water seasonality of less than one month. Despite a low accuracy on a cell basis**,** the time series analysis provides a comprehensive overview about the dominant surface water dynamics during the last three decades. In addition, the timing and the extent of flooding mirrors spatial hydroecological trends characterizing four major hydro-ecological regions:

- the endorheic valleys and dry plateaus of southern Niger,
- the Sokoto basin fed mainly by allochthone discharge from local rains on the Jos plateau,
- the semi-humid areas south of the Niger River,
- the Niger River floodplain with a bimodal flooding pattern caused by both local rains and the allochthone discharge from the Upper Niger.

2 Introduction

2.1 Technical cooperation framework

With the project *"**A**ppui à la **G**estion des **E**aux **S**outerraines dans le Bassin du Niger" (*AGES), the Federal Institute for Geosciences and Natural Resources (BGR) supports the Niger Basin Authority (NBA) in the implementation of a sustainable groundwater management. The technical cooperation project AGES is part of the "Integrated Water Resources Management NBA" program of the German Development Cooperation that comprises activities of both the Gesellschaft für Internationale Zusammenarbeit (GIZ) and the Federal Institute for Geosciences and Natural Resources (BGR) and aims specifically to:

a) institutionalize groundwater management in the framework of the NBA
b) support and establish regional, transboundary groundwater monitoring networks
c) develop methods and tools for the management of groundwater resources

The present report describes a remote sensing approach to surface water mapping in the AGES pilot zone 1, the transboundary region of Benin, Niger, and Nigeria.

2.2 Why map surface water?

Information about the spatial extent and the temporal variability of surface water is central for water management – particularly for urban and infrastructure planning, disaster prevention, and for the estimation of groundwater recharge.

Flooding and inundation are major hazards particularly in semi-arid regions with a highly erratic rainfall regime. Baseline information on the potential extent and the return period of inundation is needed to allow authorities, entrepreneurs, and households to take adequate measures to reduce the vulnerability to flooding. Via infiltration, **surface water recharges the groundwater resource**. Knowledge about the spatial extent and the temporal duration of flooding allows to estimate the magnitude of indirect, localized recharge e.g. via seasonal ponds and to evaluate its relevance compared to other means of groundwater recharge.

Digital baseline data on stream networks, lakes, and water bodies in different scales and quality is available from a variety of sources. A review of existing digital datasets available in the public domain, in general derived from topographic maps or digital elevation models, highlighted the lack of information on seasonal variability of surface water extent (chapter 9.1). Baseline data on the variability of surface water between seasons, years, and decades is, however, a prerequisite for the hazard assessment and the detection of change, the quantification of anthropogenic impact, or the influence of global climate change. Satellite imagery offers a direct mean to detect and delineate surface water bodies and monitor seasonal changes and long-term trends.

2.3 Data and methods

The assessment of a continuously changing resource such as the extent of surface water needs to be based on **statistically robust data representative for a significant period of time**. While, assessments of single satellite scenes (e.g. from a single day) or multi-temporal analyses comparing satellite scenes from different years provide static information on the state of the surface water resource, analysis of time series allows a comprehensive assessment of the dynamics of change.

Here, we apply a **time series analysis** approach based on **publicly available Landsat imagery**. The Landsat archive was selected because of the long time series (> 30 a, 1972/1984 - ongoing) and the high spatial resolution (≈ 30 m). The high spatial resolution was envisaged to allow for the detection of small seasonal ponds (< 200 m diameter) relevant for groundwater recharge, whereas the long time

series suggested a robust statistical summary. The alternative MODIS archive was deferred because of a low spatial resolution (≈ 250 m), and a short time series (1999 – ongoing) – notwithstanding a higher temporal resolution (every two days). Though being most suitable for water detection, the complex pre-processing of SAR imagery and the yet limited availability of time series barred the consideration of Synthetic Aperture Radar in the present study. From the variety of published methods and algorithms to extract surface water bodies from optical satellite images, the spectral index **Modified Normalized Difference Water Index** (MNDWI, Xu 2006) was selected.

Publicly available data, open source software, and reproducible analytical procedures allow transferring **the approach** to small-scale projects of water detection in the member states of the NBA. The approach uses open source software **QGIS** and **Python** and requires advanced **programming skills**. On the technical side, the automated processing of Landsat scenes requires large amounts of **disk space** (>1 TB) as well as processing power.

2.4 Satellite imagery and time series

Satellite imagery allows to detect and delineate surface water bodies, study surface water dynamics, and monitor seasonal changes and trends (Hansen et al. 2013; Verpoorter et al. 2014; Yamazaki et al. 2015; Donchyts et al. 2016a; Feng et al. 2016; Pekel et al. 2016). With the increasing availability of long-term time series of satellite images, particularly from the Landsat sensor family (1972 – ongoing) and the MODIS sensors (1999 – ongoing) the traditional multi-temporal comparison approach involving two or more points in time has been replaced by the analysis of entire time series. Time series moves from the qualitative comparison of surface conditions at discrete time steps to the **quantitative and statistically robust analysis of continuous data** (Tulbure & Broich 2013). The approach offers new insights into the **spatial and temporal dynamics of flooding**, thus addressing flood dynamics, seasonality, and changes of seasonal patterns. The layer stack allows the calculation of statistical summary parameters such as average, minimum, or maximum flooding extent and the detection of temporal and spatial trends for the timeframe of interest: a month, a season, a year, or the total observation period.

Within the last decade, a growing number of comprehensive time series analyses has become available. Drawing on the **long-term Landsat archive**, surface waters of Australia have been mapped on the continental scale (Tulbure 2015; Mueller et al. 2016; Sheng et al. 2016). Even more ambitious, Pekel et al (2016) analysed the entire Landsat archive on a global scale. They applied an innovative combination of expert systems, visual analytics, and evidential reasoning drawing on the spectral library and Hue-Saturation-Value (HSV) colour space classification. This high-resolution (30 m) water data set exploits the possibility of layer stack statistics and calculates not only occurrence maps but addresses also water recurrence and seasonality (https://global-surface-water.appspot.com/).

Time series analysis of the **MODIS archive** provides a higher temporal resolution of up to one day on a spatial resolution of about 250 m. Based on the MODIS data, the DLR developed the *Global Water Pack* calculated based on single-band slicing and a dynamic threshold obtained via control point comparison with a static MODIS water mask. The global product reflects the daily dynamic of inland water bodies with a resolution of 250 m (Klein et al. 2015a, 2015b, 2017).

In contrast to optical sensor (e.g. Landsat and MODIS), **Synthetic Aperture Radar (SAR)** is an active remote sensing method operating within the microwave spectra. Being independent of weather and daylight conditions, continuous and cloud-free time series analysis become possible (Lillesand et al. 2015). High resolution Synthetic Aperture Radar offers enhanced possibilities to differentiate different types of surface water, such as flooded vegetation, open water, or aquatic plants (Moser et al. 2016). In West Africa, SAR has been used local studies for example in a Multi-SAR-System to monitor lake level changes and flooding at Lake Bam, Burkina Faso (Moser et al. 2016), and Lake Tabalak, Niger (Bertram et al. 2016).

3 Environment

3.1 Study area

The AGES project focuses on a transboundary pilot zone in the border region of Benin, Niger, and Nigeria located in the Middle Niger region and comprising the Kandi Basin in Benin, the lower reaches of the nowadays-inactive palaeodrainage system of the Dallol Maouri in Niger, and the eastern part of the Sokoto Basin in Nigeria (Figure 1).

3.2 Climate

The study area falls within the Sudanian Savanna zone (moist to dry savanna) a transition zone between the Sahel (dry savanna, grasslands and scrublands) and the Guinean moist savannas in the south. It spans roughly the transition zone between the climatic dry frontier (≈ 1000 mm, evaporation equals precipitation) around Kandi and the agronomic dry frontier (≈ 500 mm, limit of rainfed agriculture) at Sokoto.

The climate is semi-arid with evaporation exceeding precipitation during 6 - 9 months during the year. Precipitation amounts diminishes by half from 1024 mm per year at Kandi, Benin (≈ 11°N), 820 mm per year at Gaya, south Niger (≈ 12°N), to 669 mm at Sokoto, northwest Nigeria (13°N) and 555 mm at Niamey, Niger, respectively (Figure 1). The number of humid months decreases from the semi-humid climate of southern Benin (5 to 6 humid months at Kandi) to only four humid months at Sokoto and Niamey. The rainy season is unimodal and starts with early rains in March/April, the first humid months in May/June and peaks in August with monthly rainfall amounts exceeding 200 mm.

3.3 Hydroecological zones

National boundaries dividing the study region roughly describe three different geoecological zones. The moist savanna south of the Niger River receives comparably high rainfall amounts (≈ 1000 mm). The main streams are perennial; tributaries are seasonal.

The dry savanna north of the Niger receives less precipitation (< 1000 mm). The fossil valleys of the now inactive former river systems Dallol Bosso and Dallol Maouri once draining the Aïr Mountains are nowadays endorheic. Locally restricted, temporal discharge occurs through flash floods, with generally no water reaching the receiving Niger River. The inactive valleys host wetland complexes with permanent often saline ponds and locally seasonal streams and creeks (Ramsar Sites Information Service 2004).

Despite a similar climate, streams of the Sokoto basin in Nigeria show a different discharge behaviour. The Sokoto River and larger streams are perennial and are fed by rainfall outside the study area in the northwestern foothills of the Jos-Plateau. Tributaries draining the low-lying areas of the sedimentary basin are seasonal (Sokoto Basin).

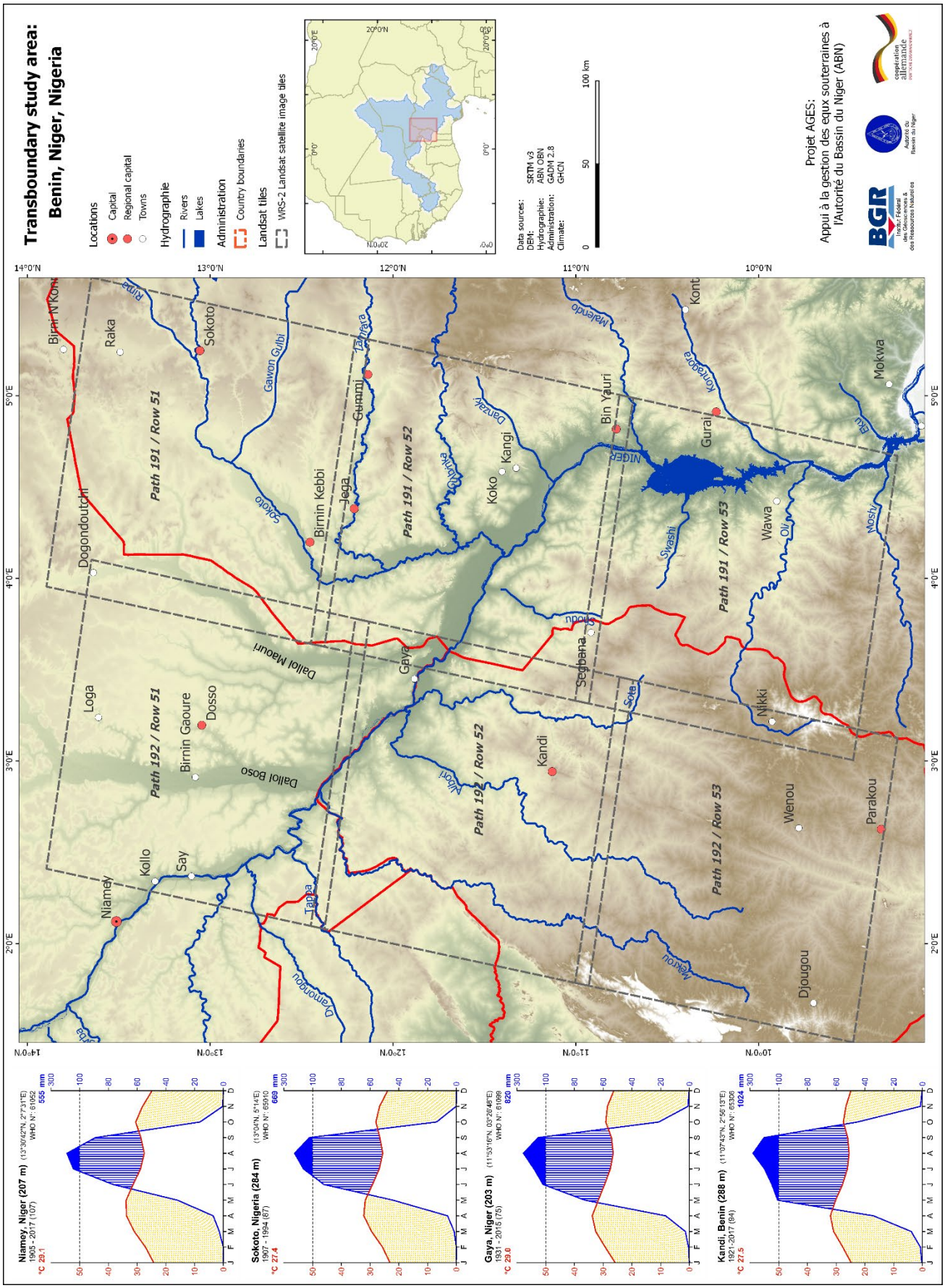

Figure 1: Transboundary study area Benin-Niger-Nigeria as outlined by six Landsat WRS-2 tiles. Representative climate graphs show the transitional character from semi-humid (southern Benin) to a semi-arid climate.

4 Water body extraction

4.1 Data: Landsat satellite imagery

4.1.1 Coverage

The Landsat satellite family offers the longest continuous global record of earth observation from space (Figure 2). This unique archive offers several advantages for long-term monitoring of surface water dynamics:

- a temporal depth of over 30 years for time series analysis,
- a high spatial resolution (30 m) for a detailed analysis,
- an archive in the public domain.

The spectral bands and their spatial resolution are comparable between Landsat sensors thus allowing direct comparison and analysis of continuous time series (Table 1). In the process of the establishment of the Landsat Collection Archive, all scenes have been reprocessed to further improve compatibility. For the future, the Landsat continuity mission aims launching compatible sensors to assure the long-term acquisition of images.

However, the USGS Landsat archive is far from being comprehensive (Kovalskyy & Roy 2013; Wulder et al. 2016). In 2016, it only contained about 1/3 of all Landsat images collected worldwide since 1972. Image acquisition was never balanced over the globe; Africa being the continent with the lowest Landsat coverage (Figure 3). Technical limitations such as battery power, duty cycles and low on-board recording capacity and prior to 1999 the lack of a systematic Landsat acquisition plan led to a distribution of scenes biased towards the United States, Australia, and China. Particularly, the low on-board recording capacity and the need for a direct transmission link of the early Landsat 1 to 5 satellites required a network of regional International Ground Control stations to receive images. Images received outside the Unites States have not systematically been incorporated into the Landsat archive. Only since 2010, the Landsat Global Archive Consolidation (LGAC) initiative begun recollecting all existing Landsat images in a single, universally accessible archive in the Earth Resources Observation and Science (EROS) Center (Wulder et al. 2016).

Generally, Landsat acquisitions follow the requests of scientific and commercial users as well as state agencies. Only with the introduction of Landsat 7 in 1999, a Long-Term Acquisition Plan (LTAP) was established with the aim to anticipate user requests and to annually cover the global land areas with

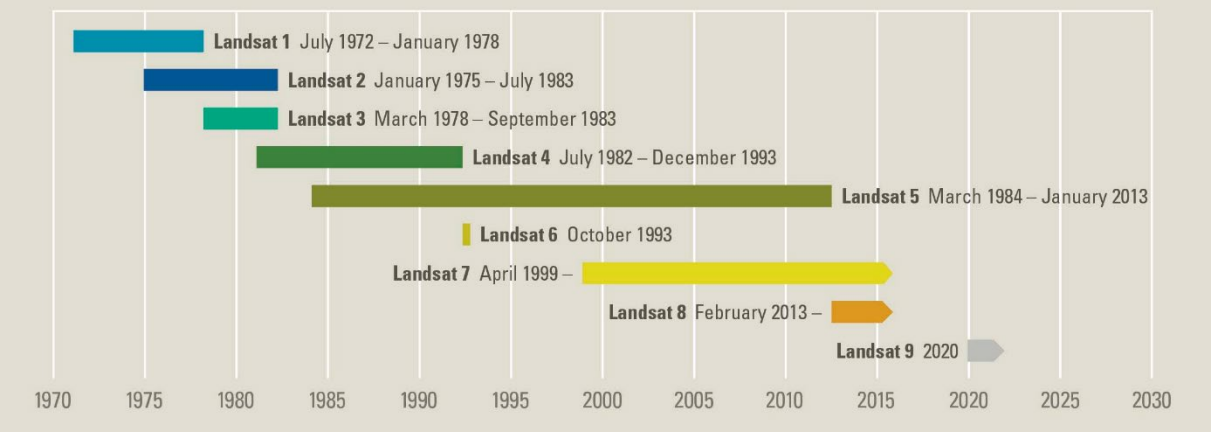

Figure 2: Landsat satellites and sensors (from USGS, 2017 at https://landsat.usgs.gov/landsat-missions-timeline).

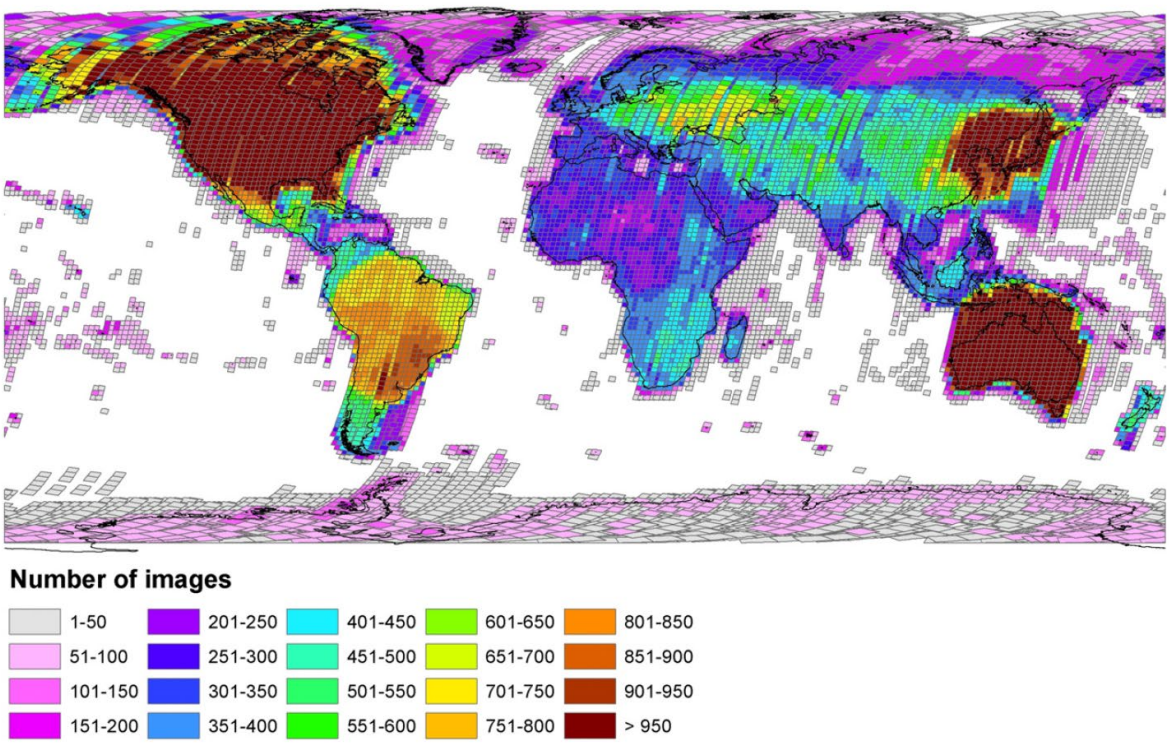

Figure 3: USGS Landsat archive holdings as of January 1, 2015 including images of Landsat missions 4, 5, 7, and 8 (from Wulder et al. 2016)

cloud-free Landsat images (Roy et al. 2010; Kovalskyy & Roy 2013). Nonetheless, the Long-Term Acquisition Plan restricts Landsat acquisitions outside the Unites States by quality properties such as cloud avoidance, seasonality, and solar zenith angle—resulting in lower numbers of acquisitions for areas with a frequent cloud cover. Following Figure 3, West Africa is one of the regions with the lowest Landsat coverage ranging between 200 and 350 available Landsat images up to 2015. Since the launch of Landsat 8 in 2013, coverage over West Africa increased significantly (cf. chapter 5.1).

4.1.2 Data specifications

Complete time series of Landsat 4 & 5, Landsat 7, Landsat 8 Surface Reflectance Data, also known as Climate Data Records (CDR), were selected from the USGS Landsat Archive via the Earth Explorer interface (https://earthexplorer.usgs.gov/). The search results were exported as a list of scenes (.csv), processed to contain only scene identifiers, and uploaded via the On-Demand interface of the USGS EROS Center (Earth Resources Observation and Science) Science Processing Architecture (ESPA) (https://espa.cr.usgs.gov/). Download links are provided that allow download of the Surface Reflectance Climate Data Records via a browser specific bulk download application.

All selected scenes are Level 1 precision- and terrain-corrected (L1T) and include radiometric and geodetic corrections based on both ground control points and a digital elevation model. Data specifications of the surface reflectance data for Landsat 7 scenes are shown in Table 8 (Appendix). In the present study, we accessed the Pre-Collection Archive. Since 2016, the Landsat archive has been restructured. Future studies will have to rely on the new, tiered collection (https://www.usgs.gov/land-resources/nli/landsat/landsat-collection-1).

Spectral Region	Abbrev.	Multispectral Scanner (MSS) 1972 - 1983				Landsat Thematic Mapper™ 1982 - 2013			Enhanced Thematic Mapper Plus (ETM+) 1999 -			Operational Land Imager (OLI) & Thermal Infrared 2/2013 -			Use & Interpretation
		Landsat 1, 2 & 3	Landsat 4 & 5	Wavelength [µm]	Resolution [m]	Landsat 4 & 5	Wavelength [µm]	Resolution [m]	Landsat 7	Wavelength [µm]	Resolution [m]	Landsat 8	Wavelength [µm]	Resolution [m]	
Ultra Blue	**Ultra Blue**											band 1	0.43 - 0.45	30	Coastal aerosol
Visible Light	**Blue**					band 1	0.45-0.52	30	band 1	0.45-0.52	30	band 2	0.45 - 0.51	30	Bathymetric mapping, distinguishing soil from vegetation and deciduous from coniferous vegetation
	Green	band 4	band 1	0.5-0.6	60 [1]	band 2	0.52-0.60	30	band 2	0.52-0.60	30	band 3	0.53 - 0.59	30	Emphasizes peak vegetation, which is useful for assessing plant vigor.
	Red	band 5	band 2	0.6-0.7	60 [1]	band 3	0.63-0.69	30	band 3	0.63-0.69	30	band 4	0.64 - 0.67	30	Sediment-laden water, delineates areas of shallow water Discriminates vegetation slopes. Cultural features
Near Infrared	**NIR**	band 6	band 3	0.7-0.8	60 [1]	band 4	0.76-0.90	30	band 4	0.77-0.90	30	band 5	0.85 - 0.88	30	Emphasizes biomass content and shorelines
Shortwave Infrared	**SWIR 1**	band 7	band 4	0.8-1.1	60 [1]	band 5	1.55-1.75	30	band 5	1.55-1.75	30	band 6	1.57 - 1.65	30	Discriminates moisture content of soil and vegetation; penetrates thin clouds
	SWIR 2					band 7	2.08-2.35	30	band 7	2.09-2.35	30	band 7	2.11 - 2.29	30	Improved moisture content of soil and vegetation and thin cloud penetration. Hydrothermally altered rocks associated with mineral deposits
Panchromatic	**PAN**								band 8	0.52-0.90	15	band 8	0.50 - 0.68	15	15 meter resolution, sharper image definition
SWIR 1	**Cirrus**											band 9	1.36 - 1.38	30	Improved detection of cirrus cloud contamination
Thermal Infrared	**TIRS 1**					band 6	10.40-12.50	120 [2] (30)	band 6	10.40-12.50	60 [3] (30)	band 10	10.60 - 11.19	100 [4] (30)	Thermal mapping and estimated soil moisture
	Tirs 2											band 11	11.50 - 12.51	100 [4] (30)	Improved thermal mapping and estimated soil moisture

[1] Original MSS pixel size was 79 x 57 meters; production systems now resample the data to 60 meters.
[2] TM band 6 was acquired at 120-meter resolution, but products are resampled to 30-meter pixels.
[3] ETM+ band 6 is acquired at 60-meter resolution, but products are resampled to 30-meter pixels.
[4] TIRS bands are acquired at 100 meter resolution, but are resampled to 30 meter in delivered data product.

Table 1: Sensor specifications Landsat 1-8 (adapted from https://landsat.usgs.gov/what-are-band-designations-landsat-satellites, USGS, 12/2016)

4.2 Method: MNDWI a spectral indices for surface water detection

4.2.1 Principle of surface water detection using optical sensors

Water detection using optical sensors is based on the distinct spectral signature of clear water, vegetation, and soil to discriminate between land and water (Figure 4). Clear water strongly absorbs radiation of light with wavelengths beyond > 600 nm and moderately reflects wavelengths of the visible light (Lillesand et al. 2015). The absorption capacity of water changes according to the sediment load, chlorophyll concentrations, the texture of the water surface, and surface contamination. For example, turbid water as well as water with a higher amount of biota or a high chlorophyll concentration show an enhanced reflectance in the visible light compared to clear water. Further, contamination of the water surface by e.g. wastewater or oil spills may change the spectral reflectance characteristics, complicating automated detection.

Vegetation, on the other hand, predominantly absorbs radiation in the visible spectra and reflects in general most of the infrared light. The spectral signature of soils varies according to moisture content, soil texture, surface roughness, organic matter, and particularly mineral content (e.g. iron oxides) (Lillesand et al. 2015).

The high absorption/low reflection properties of water at near-infrared wavelengths and opposing trends of absorption/reflection for vegetation and soil are the general principles for the detection and delimitation of water bodies using optical satellite imagery (Figure 4). The following paragraphs present two selected approaches—spectral indices and single band thresholding to detect surface water using the characteristic spectral signature of water.

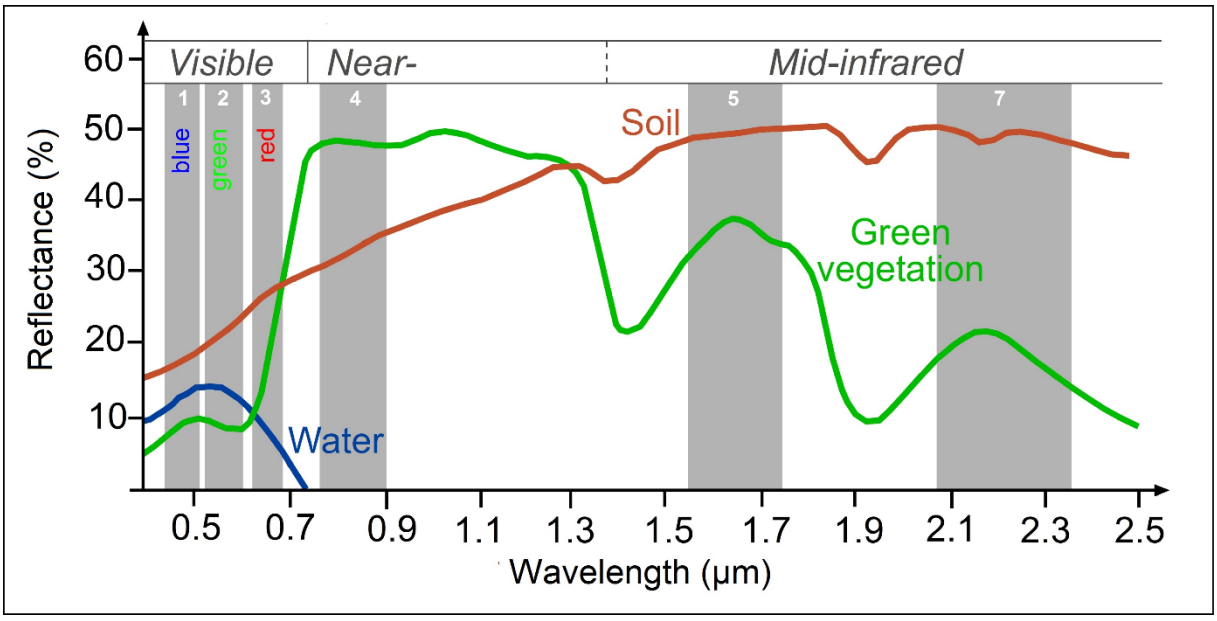

Figure 4: Spectral reflectance of clear water, green vegetation, and an exemplary soil at different wavelengths. Landsat TM channels are shown (SEOS, 2016: http://www.seos-project.eu/modules/classification/classification-c01-p05.html)

4.2.2 Single band thresholding / Density slicing

Single band thresholding or density slicing is a straightforward method that takes advantage of the characteristic absorption spectrum of water in the infrared spectrum. A single short wave infrared band—generally SWIR 1 or SWIR 2—is used to discriminate between water and land. The approach has been used, for example in regional studies on the Logone floodplain in Chad (Westra & De Wulf 2009; Jung et al. 2011; Wilczok 2014) but also on a global scale for the calculation of the Global WaterPack by the DLR (Klein et al. 2015a).

4.2.3 Spectral Indices

One of the most common approaches to water body extraction is the use of spectral indices. Spectral indices compare the spectral signature of water and non-water areas (vegetation and soil) to identify water areas. The use of two spectral bands—in comparison to only one band for density slicing—enhances the contrast of the water signal.

Indices range from **simple ratios** between two bands to complex mathematic formulas using different spectral bands. Prominent are **Normalized Difference Indices** that divide the difference between two specific bands by their sum. Normalization reduces the effect of variable irradiance (image brightness) by rescaling the data to a range from -1 to +1.

For the detection of surface water, an **infrared band** is used **for water detection** and a band of the **visible light for normalization**. Positive index values indicate water characterized by high reflectance values in the visible light and low reflectance values in the infrared spectra. Negative index values suggest land areas (mixture between vegetation and soil) with low reflectance in the visible light and high reflectance in the infrared region.

$$Normalized\ Difference\ Index\ = \frac{visible - infrared}{visible + infrared}$$

Table 2: Selected spectral indices used for water body extraction (Rouse 1974; McFeeters 1996; Wilson & Sader 2002; Rogers & Kearney 2004; Xu 2006; Shen & Li 2010; Boschetti et al. 2014; Feyisa et al. 2014)

Authors	Year	Index	Sensors	Spectral bands	Index	Standard threshold
Rouse	1974	**NDVI** Normalized Difference Vegetation Index	Landsat	red, NIR (band 2 & 1)	$NDVI = \frac{NIR - RED}{NIR + RED}$	<0
McFeeters	1996	**NDWI** Normalized Difference Water Index	Landsat	green, NIR (band 2, band 4)	$NDWI = \frac{GREEN - NIR}{GREEN + NIR}$	>0
Wilson & Sader	2002	**NDMI** Normalized Difference Moisture Index	Landsat	NIR, SWIR 1 (band 4 & 5)	$NDMI = \frac{NIR - SWIR\,1}{NIR + SWIR\,1}$	>0
Rogers & Kearny	2004	**NDWI** Normalized Diff. Water Index (modified)	Landsat	red, SWIR 1 (band 3, band 5)	$NDWI_2 = \frac{RED - NIR}{RED + NIR}$	>0
Xu	2006	**MNDWI** Modified Normalized Difference. Water I.	Landsat	green, SWIR 1 (band 2, band 5)	$MNDWI = \frac{GREEN - SWIR\,1}{GREEN + SWIR\,1}$	>0
Shen & Li	2010	**WRI** Water Ratio Index	Landsat	green, red, NIR, MIR	$WRI = \frac{Green + Red}{NIR + MIR}$	>1
Boschetti et al.	2014	**NDFI** Normalized Difference Flood Index	MODIS	blue, SWIR 2 (MODIS band 1 & 7)	$NDFI = \frac{BLUE - SWIR\,2}{BLUE + SWIR\,2}$	>0
Feyisa et al.	2014	**AWEI** Automated Water Extraction Index	Landsat	Blue, green NIR, SWIR 1 bands 1, 2, 4, 5, 7	$AWEI_{nsh} = 4(\rho_{band2} - \rho_{band5}) - (0.25 \times \rho_{band4} + 2.75 \times \rho_{band7})$ $AWEI_{sh} = \rho_{band1} + 2.5 \times \rho_{band2} - 1.5 \times (\rho_{band4} + \rho_{band5}) - 0.25 \times \rho_{band7}$	<0

4.2.4 Modified Normalized Difference Water Index (MNDWI)

Boschetti et al. (2014) evaluated 11 spectral indices and reports best classification results for the Modified Normalized Difference Water Index (MNDWI) that even performs in highly vegetated water. The original Normalized Difference Water Index (NDWI) uses the ratio between green and the near infrared light (NIR) (McFeeters 1996). An adaption by Rogers and Kearny (2004) uses the red and the middle or first short-wave infrared light (abbreviated: SWIR 1 or sometimes MIR for middle infrared, see Figure 5), whereas the **Modified Normalized Difference Water Index (MNDWI)** suggests a combination of the green and the first short-wave infrared light (SWIR 1) (Xu 2006; Du et al. 2016).

$$NDWI = \frac{Green - NIR}{Green + NIR} \qquad MNDWI = \frac{Green - SWIR1}{Green + SWIR1}$$

Other spectral indices for water detection have been proposed (Table 2), each adapted to a special environment or developed to overcome existing shortcomings (see Liu et al. 2016). Particularly, cloud shadows, shadows in mountainous areas, and the reflection signal from smooth build-up, artificial surfaces cause problems in the identification of open water bodies (Gao et al. 2016). To increase spectral separability between water, shadows, and build-up areas, Feyisa et al. (2014) for example suggested two Automated Water Extraction Indices (AWEI) for shadow and non-shadow areas. Further methodologies, for example Boschetti et al. (2014) for the MODIS sensor propose indices to separate between land (soil and vegetation), flooded vegetation and water via a normalized difference of blue and the second short-wave infrared light (SWIR2) .

The present study applied the **Modified Normalized Difference Water Index**. Its **simple structure** facilitates a **comparable rapid processing** of the time series with **large amounts of data** (> 1000 scenes for the study area) without the need of high-performance programming.

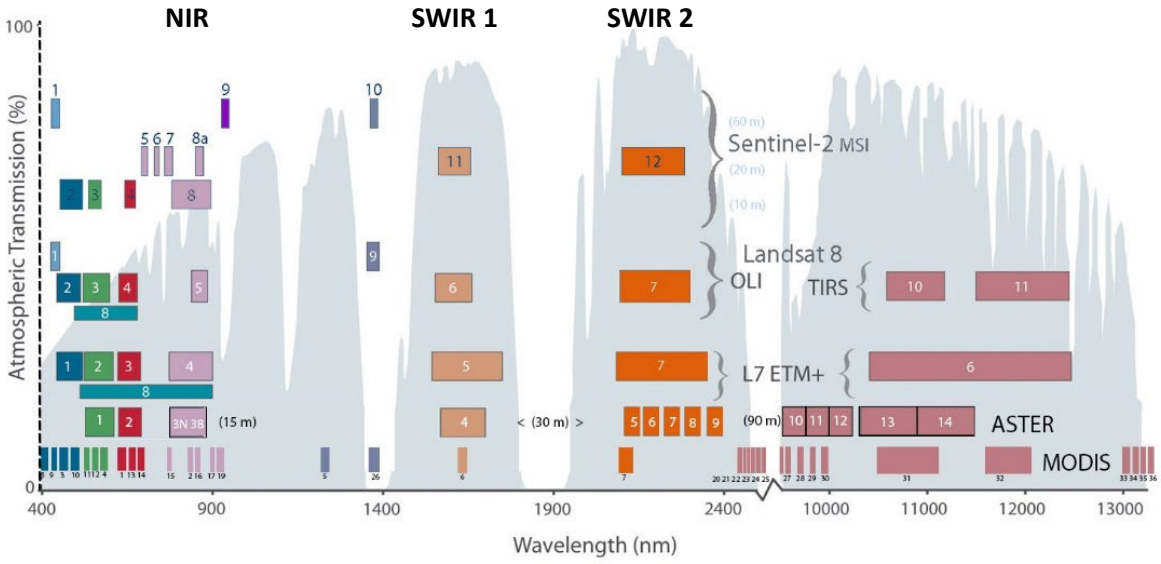

Figure 5: Atmospheric transmission spectrum and spectral windows of a selection of sensors (adapted from USGS, 2016, pic.twitter.com/6GJ3mtEWKX)

4.3 Processing

The MNDWI is calculated using three input parameters: two spectral bands –visible light in the range between 0.5 and 0.6 µm, commonly referred to as green light, and the first short-wave infrared light (SWIR 1) – and the USGS cloud mask (CFmask) that allows masking of cloud and shadow areas. The automated workflow followed three main steps (Figure 6):

1. Masking of distorted cell values for each single scene using the respective CFmask
2. Calculation of the MNDWI for each single scene
3. Calculation of spatial and temporal statistics

Caution is necessary as the number of bands, band numbers, denomination of both spectral ranges and bands (e.g. SWIR 1, MIR), and to a minor extent even the spectral ranges of bands differ between the three Landsat sensors (cf. Table 3).

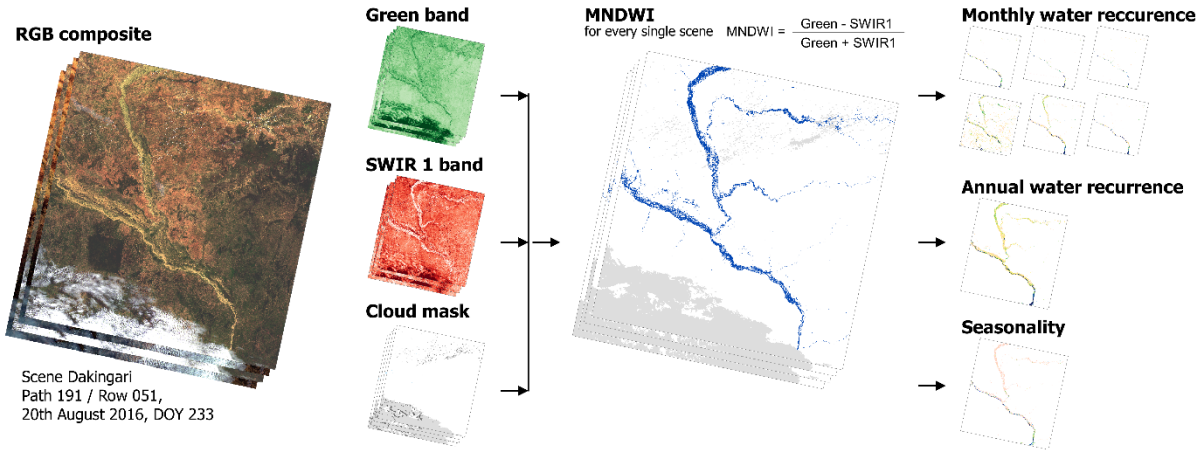

Figure 6: Water body extraction workflow: MNDWI values are calculated based on three input parameters—Green (visible light ca. 0.5-0.6µm), SWIR 1, and the cloud mask (CFmask). Based on cell statistics, probability of monthly and annual flooding and surface water seasonality are calculated.

Table 3: Landsat sensors, band designations, and respective wavelengths. Compiled from USGS (https://landsat.usgs.gov/what-are-band-designations-landsat-satellites).

Sensor	Green		Shortwave Infrared (SWIR) 1	
	Wavelength [µm]	Band	Wavelength [µm]	Band
Landsat 4-5 TM	0.52-0.60	band 2	1.55-1.75	band 5
Landsat 7 ETM+	0.52-0.60	band 2	1.55-1.75	band 5
Landsat 8 OLI	0.53 - 0.59	band 3	1.57 - 1.65	band 6

4.3.1 Masking

Masking is necessary as the original Landsat image includes areas (cells, pixels) that do not provide reliable information. Distorted values may result from atmospheric conditions (e.g. clouds), land covers with a high reflectance (snow-covered areas, some bright soils, water), and adverse sensor geometry (e.g. specular reflection or hotspot reflection)—or a mixture of the above—causing general radiometric saturation at the sensor.

The respective cells are masked and excluded from analysis. As part of the Surface Reflectance Data product, the USGS provides a pre-processed CFmask (C Function of Mask algorithm, also referred to as USGS cloud mask) that identifies high reflectance values and provides five categories: clear (0), water (1), cloud shadow (2), snow (3), cloud (4). Only cells flagged as “clear” or “water” are included in the analysis. However, the CFmask does not identify all cases of intensive radiometric saturation, which caused visually obvious misclassifications in the present study. The present study only considered band values falling within the valid range of the Surface Reflectance Data products specified to range between 0 - 10.000 (Landsat Product Guides (USGS 2016a, 2016b).

The CFmask provides a surface water class. However, this water mask is conservative and high omission errors have been observed during the preparatory work of this study. In consequence, the provided CFmask is not suitable for the purpose of monitoring surface water or stream network extraction.

4.3.2 Threshold

The main challenge using spectral indices (and density slicing) for surface water detection is the setting of a suitable threshold separating water and non-water. By definition, Normalized Difference Indices range from -1 to +1 and by their structure suggest a threshold of zero (McFeeters 1996): positive values—in the case of the MNDWI a low reflection of the shortwave infrared compared to the green light—indicating open water surfaces. This standard threshold may lead to both over—or underestimation of water bodies (Liu et al. 2016). Most studies focusing on a single pilot zones manually adjust this threshold to a visually delimited water surface derived from an RGB composite (Feyisa et al. 2014; Liu et al. 2016) or, less frequently, according to ground-truthed control points. An reproducible and automated approach is put forward by the Global Water Pack (Klein et al. 2015a) that uses a static water mask derived from the global MODIS44W water mask (Carroll et al. 2009) to provide training areas.

This study, adopted the standard threshold 0 (zero) of the MNDWI. Time series record seasonal variation of environmental conditions (soil moisture, soil cover, vegetation density and greenness, (water) surface roughness, etc…) that further introduces a variability in time and space to the spectral reflectance signal of the land and water surfaces. Approaches to identify suitable thresholds for spectral indices include supervised classifications, adaptive threshold algorithms, image segmentation, and histogram segmentation. Due to time and programming constraints, these were beyond the means of the project. A preliminary study (results not shown), showed that image enhancement techniques such as a dynamic Otsu (cf. Yang et al. 2014; Donchyts et al. 2016b) were not adequate to overcome the obstacles of the heterogeneous land cover and the strong environmental gradient in the study area.

5 Results

Seasonal and annual surface water dynamics are described by the following four parameters that condense the information from the 1756 single scenes spanning 32 years of observation (1984 - 2016):

- Number of valid observations
- Probability of annual flooding (annual water recurrence)
- Probability of monthly flooding (monthly water recurrence)
- Surface water seasonality (duration of flooding)

The parameters are calculated based on the number of available valid observations per year/month. Any interpretation has to take into account the uneven temporal (monthly, seasonally, yearly) acquisition of scenes and the high number of years/months without observation.

5.1 Number of observations

Six Landsat tiles were analysed (Table 4), each with between 274 and 326 single satellite image scenes from the sensors Thematic Mapper (TM, Landsat satellites 4 & 5, 1982 - 1983 & 1984 - 2013), Enhanced Thematic Mapper Plus (ETM+, Landsat 7, 1999 - 2016 mission ongoing) and Operational Land Imager (OLI, Landsat 8, 2013 - 2016 ongoing).

The number of valid observations on a cell basis is restricted by:

1. spatial and temporal availability of Landsat scenes following the Landsat mission acquisition plan and technical issues. (cf. chapter 4.1.1)
2. cloud cover during the rainy season (cf. chapter 4.3.1

Sensor type (TM, ETM+, OLI) and **temporal coverage** varied during the observation period from 1984 to 2016 as exemplary shown in Figure 7 for the tile 192/51 (Dosso, cf. Appendix 9.3 for the other tiles). During the early phase (1984 to 1988), Landsat satellites 4 & 5 acquired a low and variable number of scenes per year. A low number of scenes per year (generally < 10) were acquired in the period 1986-1990 with years of no image acquisition in the period 1991 - 1997. Following the launch of Landsat 7 ETM+ in 1999, a more constant coverage between 3 and 15 scenes per year and tile was possible. It was not until the launch of Landsat 8 OLI in 2013, when a full annual coverage with about 30 scenes per year became available.

The **seasonal distribution** of acquired scenes is skewed towards the dry season (Figure 8 cf. Appendix 9.3 for other tiles)—among others (cf. 4.1.1) a direct consequence of the acquisition plan of the Landsat mission intentionally and systematically restricting image acquisition to cloud-free images (Ju & Roy 2008).

Within a scene, **cloud cover** further reduces the number of valid observations per cell. Figure 10 visualizes the number of valid observations and their spatial monthly distribution. The extreme low number of valid observations (often less than 5) in the southern tiles 192/53 (Bembérèke) and 191/53 (Kainji) leads to obvious erroneous results such as an apparently high percentage of annual flooding induced by a single observations—to the extreme that for some cells no observations for the month of August are available at all.

The low number of available scenes, the skewed seasonal availability of scenes, and the high cloud coverage result in a low temporal and spatial coverage of valid observations particularly for the rainy season—the main period of interest for the detection of flooding and temporal water body formation.

Table 4: Landsat sensors and respective number of scenes per tile.

Tile		Satellite & Sensor				
		Landsat 4	Landsat 5	Landsat 7	Landsat 8	
N°	Name	TM		ETM+	OLI	Total
192/51	Dosso	12	49	184	81	**326**
192/52	Kandi	8	44	180	79	**311**
192/53	Bembérèke	10	26	171	67	**274**
191/51	Birnin Kebbi	4	47	163	76	**290**
191/52	Dakingari	2	33	181	78	**294**
191/53	Kainji	2	20	166	73	**261**
		38	219	1045	454	**1756**

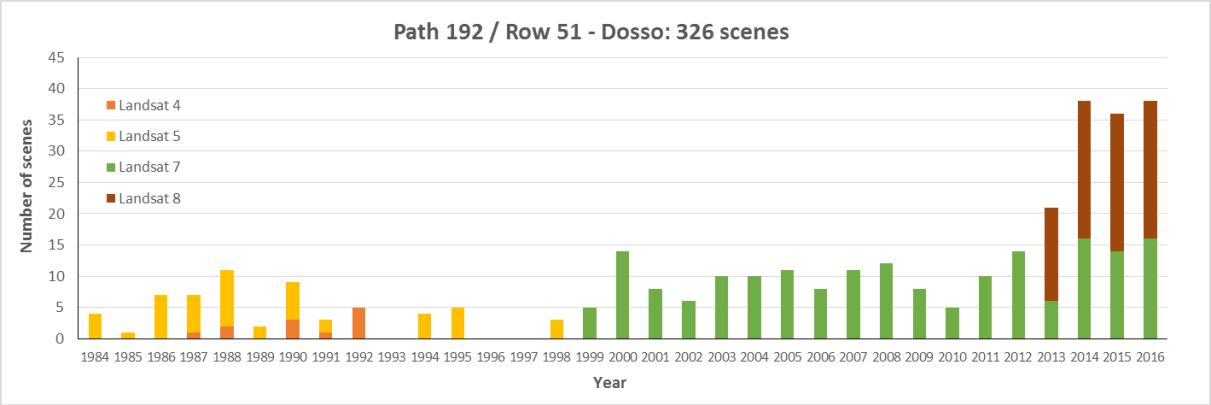

Figure 7: Sensor type and number of available scenes between 1984 and 2016 for the tile 192/51 (Dosso).

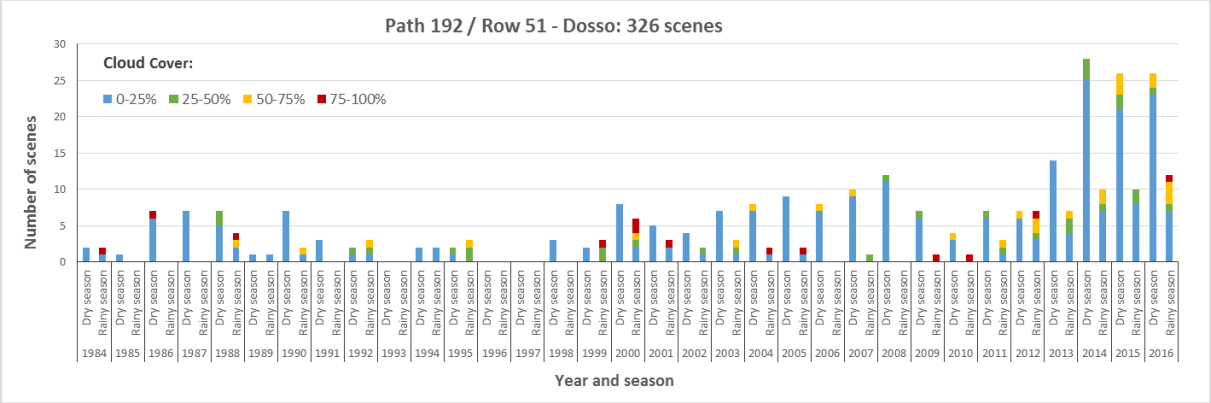

Figure 8: Seasonal distribution and cloud cover for available satellite scenes of tile 192/51 (Dosso). Rainy seasons spans the four months June, July, August, and September.

5.2 Probability of annual flooding (annual surface water recurrence)

Probability of annual flooding is the **inter-annual surface water variability** for the years 1984 - 2016. The probability or frequency of annual flooding is calculated as the ratio between the number of years with at least one flooded scene and the number of observed years between 1984 and 2016. It is expressed either as frequency of flooding within the observation period or as the corresponding water recurrence interval

$$probability\ of\ annual\ flooding = \frac{\sum years\ flodded\ once}{\sum years\ observed}$$

As water recurrence, it describes the **recurrence interval of the respective flood extent** (F_{10}). It is important to note, that the maximum flood extent corresponding to a specific recurrence interval cannot be correlated with the peak flood discharge (e.g. Q_{10}). The maximum annual/monthly flood extent calculated from a time series is a statistical summary extent overestimating the area flooded at any given time. Areas that have been prone to flooding are categorized into three groups (see Table 6, Figure 11 to Figure 16):

- **Reliably flooded areas** show surface water in 90 % to 100 % of the years observed and are flooded (almost) every year. They comprise both perennial water bodies and inundation areas. With an extent of about 1,414 km², they cover 0.8 % of the total study area (175,763 km²).
- **Variably flooded areas** are divided into three categories:
    1) areas flooded regularly every other year. With a recurrence interval of less than two years, areas flooding in 50 % to 90 % of the years observed cover an area of about 423 km² (0.24 % of the study area).
    2) areas flooded at least once in 5 years. Areas with a water recurrence interval of 2 to 5 years (20 % - 50 % of years observed) comprise about 1,695 km² (0.81 %).
    3) areas flooded at least once every 10 years. About 1,185 km² (0.68 % of the study area) are flooded in 10 % - 20 % of all year observed corresponding to return periods of 5 to 10 years.
- **Rarely flooded areas** are flooded less than once in 10 years (< 10 % of observed years). Covering 11.5 % of the study area (20,065 km²), this category is quite extensive due to two reasons: first, it summarizes all minor, short-lived, or erratic flood events that occurred in the given period. Second, such short-lived flood events are prone to misclassifications. Misclassifications may arise a) statistically from low numbers of valid observations, b) from the applied standard MNDWI threshold or c) from erroneous cloud masking or distorted reflection values directly influencing a) and b).
  Rarely flooded areas occur more often in areas south of the Niger River. Here, the low number of available scenes (cf. Figure 10; Figure 11; Figure 16) and a more humid climate allowing for a denser vegetation with a higher plant water content facilitate incidences of misclassification. The category “rarely flooded areas” is particularly prone to such misclassifications and thus provides only very poor information on the risk of flooding. This category should not be over interpreted.
- **No observations** result from either persistent cloud cover and/or erroneous cloud masks for the available satellite images. High cloud coverage during the rainy season—particularly in tiles 192/53 (Bembérèke) and 191/53 (Kainji)—are responsible for high numbers of invalid observations in July and August.

With respect to the mentioned limitations, the maximum extent of potentially flooded areas in the observation period can be assumed as 24,782 km² corresponding to about 14 % of the study area.

5.3 Probability of monthly flooding (monthly water recurrence)

Probability of monthly flooding describes the **inter-annual variability of water occurrence per month** between 1984 and 2016. Probability of monthly flooding is calculated as the ratio between the number of years with at least one flooded scene during the respective month and the number of years with valid monthly observations. The ratio describes the probability of flooding on a monthly basis. If a given area was not observed in a given month, the respective year is not taken into account. Probability of monthly flooding highlights areas where flooding in the respective month has to be expected.

$$probability\ of\ monthly\ flooding\ = \frac{\sum years, month\ flodded\ once}{\sum years, month\ observed}$$

During the rainy season, the ***reliably flooded surface water area*** (90 - 100 % of years observed) increases from a minimum of 872 km² (surface water extent in June)—to a maximum of about 2,161 km² in August (5.9 % of study area, Table 6). However, a small second maximum can be observed from November (1,449 km²) until January with a similar area flooded. This second, small, but prolonged water surface maximum is the result of the so-called "Guinean flood" of the Niger River. The "Guinean flood" results from the arrival of waters from the rainy season in headwaters of the Niger, in Guinea, Ivory Coast, and southern Mali—delayed due to its passage through the flat Niger inland delta in Mali (cf. Figure 13).

The ***variably flooded surface water extent*** (10 - 90 % of years observed) records predominantly inundations caused by the local rains. In general, these areas show a rapid rise in July, a pronounced single peak in August, and slowly receding flood areas in September to November. A second peak associated with the "Guinean flood" is not observed suggesting that the extent of the "Guinean flood" is comparatively reliable and does not vary strongly between years probably because of the spatial restriction to the Niger floodplain.

Rarely flooded areas are inundated in less than 10 % of the years observed. The maximum extent is shown for September to October—about one to two months later than the peak indicated by both the reliably and the variably flooded areas. Given the limitations discussed for the annual probability of flooding, a tentative interpretation of this observation might be that the onset of the rainy season and the early flooding are relatively reliable whereas the duration and cessation of rains show a higher variability resulting in larger extents of rarely flooded areas at the end of the rainy season.

Conspicuous are large but rarely flooded areas in March and May (cf. Table 6 & Figure 9) that are not related to the "Guinean flood" and that cannot be correlated with a local rainfall peak. Not reflected in the rainfall data (cf. Figure 1), the incipient rainy season in May is locally identified as a small rainfall peak known as "mango rains" (***Pluie de mangue***). The observed increase of the flooding extent is tentatively related to the *Pluie de manque*. Yet, erroneous classification or cloud mask problems in combination with low numbers of observations numbers caution that the observed flooding extent does not necessarily reflect the real surface water conditions.

5.4 Seasonality

Seasonality describes the **intra-annual variability** of surface water extent for an average year between 1984 and 2016. Calculated as the sum of the monthly flood probability, it provides the **number of months per year an area is flooded**. Estimating the average duration of flooding, seasonality is a suitable parameter to discriminate between permanent and seasonal water bodies (Figure 17, Table 5).

$$\sum probability\ of\ monthly\ flooding$$

Permanent water bodies flooded for 12 months a year amount to about 702 km² with an additional 2,634 km² of ***seasonally flooded areas*** between 1 and 11 months. Most of the seasonally flooded areas are only flooded less than 4 months (1,736 km²) during the ***local rainy season***. Areas being flooded between 5 and 9 months likely represent the large Niger floodplains flooded by both the local "red flood" and the "Guinean flood". Large areas are flooded between 10 to 11 months (425 km²) and only fall dry at the end of the dry season. These areas likely belong to the main area of ***streams and rivers***.

Not considered are **areas flooded for less than 1 month** (21,432 km²). These comprise potentially flood-prone areas in major and minor river floodplains, the drainage system of the Dallols, and streams. Given the comparable small size of even the Niger tributaries around or below the sensor resolution of 30 m, these water bodies are not clearly defined by the MNDWI algorithm due to the not further investigated mixed pixel effect—a raster cell covering both water and land areas producing a mixed spectral signature prone to misclassification.

5.5 Permanent water bodies

The extent of permanent water bodies delineated by either seasonality or probability of flooding differs by about 10 %. Probability of flooding suggests an **average minimum surface water extent** at the end of the dry season with 872 km² (June), respective 979 km² (July); about 0.5 % of the study area (Table 6). Permanent water bodies are delineated by the extent of surface water at the end of the dry season. Major drawback is the variability of the onset of the rainy season. Whereas early and erratic precipitation events may occur as early as April and intensify during May, the average minimum surface water extent regarding the entire study area is observed with a time lag in June (Figure 11 to Figure 16, Table 6). The arbitrary selection of June as the month with the smallest overall surface water extent and the averaging of the variable water extent over the time series overestimate the final guess of the surface water area.

Seasonality, on the other hand, is a conservative and probably more reliable descriptor of permanent water bodies. Seasonality assess **the annual duration of flooding** with permanent water bodies (i.e. being flooded for 12 months a year) calculated to only 702 km² (Table 5). It averages the yearly duration of flooding, only including areas with continuous surface water coverage. The resulting smaller extent of permanent water bodies is more robust against false positives.

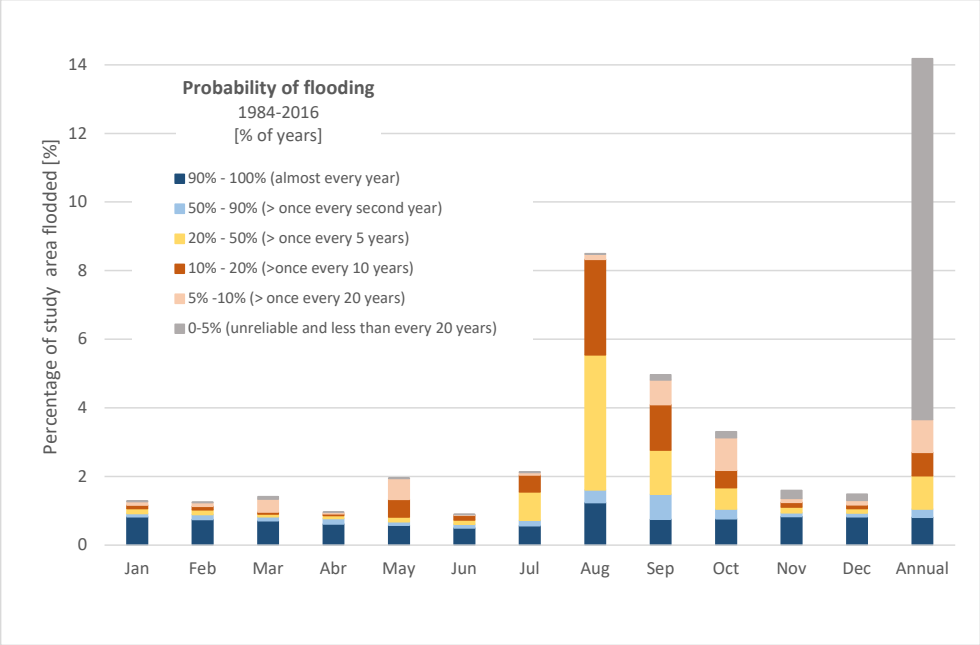

Figure 9: Probability of flooding: Extent and frequency of surface water occurrence.

Table 5: Seasonality. Average duration of flooding and respective average water extent 1984 - 2016. The reported water extents are average values over the study period and should only be used to indicate the order of magnitude of flooding.

Duration of flooding (1984 - 2016)			Area flooded [km²]	[%]
(non-flooding)		0 months	149.206	85,38
seasonally flooded areas (2,634 km²)	unreliable	< 1 month	21.432	12,26
	local rainy season (1,736 km²)	2 months	1303	0,75
		3 months	315	0,18
		4 months	118	0,07
	prolonged flooding (473 km²)	5 months	74	0,04
		6 months	63	0,04
		7 months	88	0,05
		8 months	120	0,07
		9 months	128	0,07
	streams (425 km²)	10 months	110	0,06
		11 months	315	0,18
permanent water bodies		12 months	702	0,40
		no observations	789	0,45
			174.763	100,00

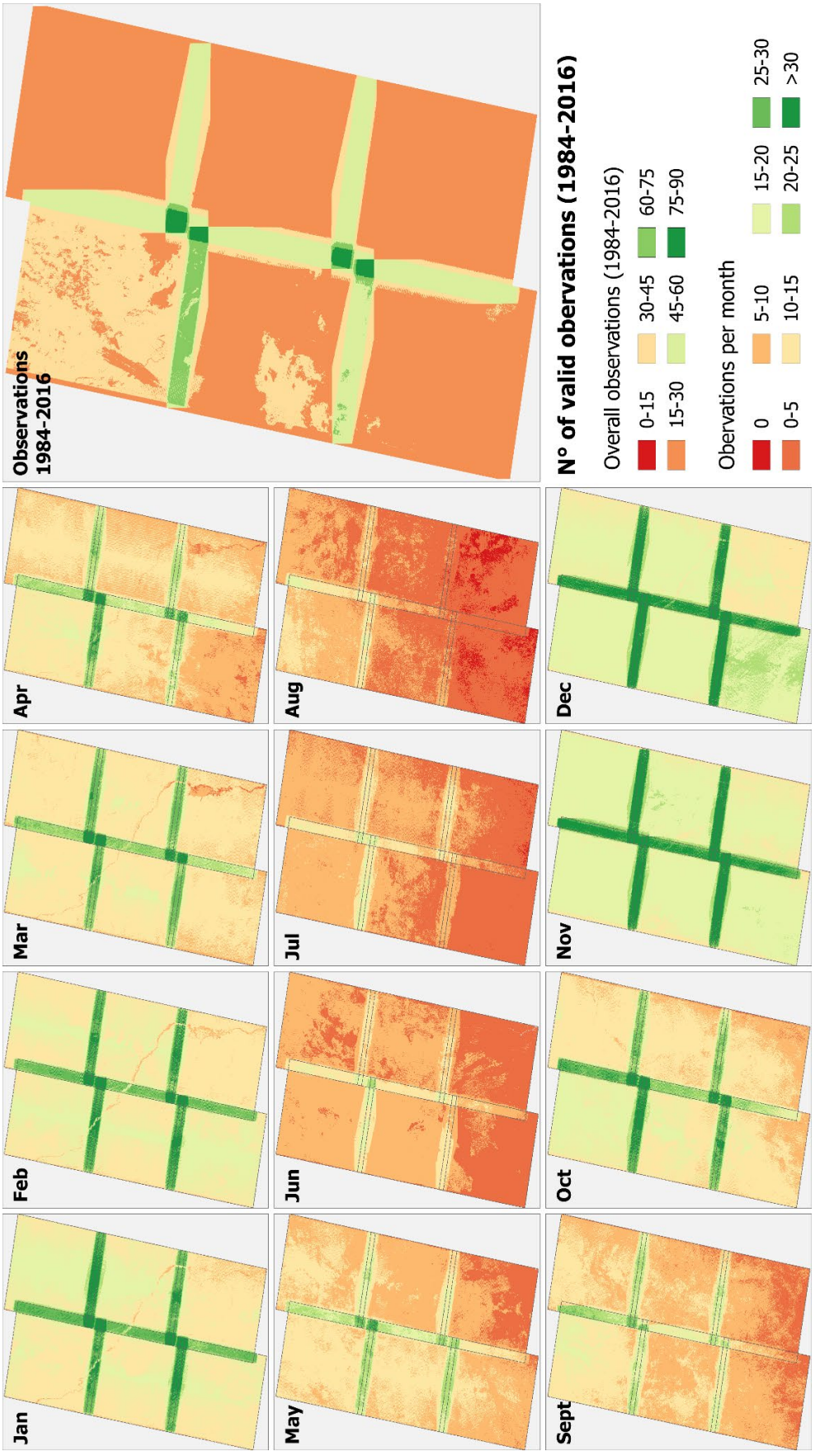

Figure 10: Number of valid observations (1984 - 2016) for monthly and annual analyses. Low numbers of observations are observed in the rainy season due to persistent cloud cover.

a) Average surface area [km²]

	Recurrence interval (1984-2016)		Flooding probability	Jan	Feb	Mar	Apr	May	Jun	Jul	Aug	Sept	Oct	Nov	Dec	Annual
						erratic rains		Rainy season					erratic rains			
	no flooding observed		0%	172.517	172.570	172.300	173.080	171.337	173.173	170.360	149.592	166.050	168.992	171.938	172.172	149.942
water surface: rarely flooded or unreliable	$F_{<20}$	< once in 20yrs	<5%	37	28	118	10	27	1	35	20	277	296	414	316	18.386
	F_{10-20}	> once in 20yrs	5-10%	171	198	658	74	1.066	37	135	267	1.256	1.667	204	224	1.679
water surface: variably flooded	F_{5-10}	> once in 10yrs	10-20%	174	167	109	83	900	239	852	4.864	2.315	882	234	191	1.185
	F_{2-5}	> once in 5yrs	20-50%	254	251	142	151	240	213	1.449	6.884	2.240	1.088	294	234	1.695
	$F_{>2}$	> once in 2yrs	50%-90%	174	254	201	278	176	187	282	645	1.279	493	192	189	423
water surface: reliably flooded	F_0	every year	90%-100%	1.435	1.294	1.234	1.077	1.009	872	979	2.161	1.314	1.344	1.449	1.435	1.414
	flooded total		>0%	2.245	2.192	2.462	1.673	3.418	1.549	3.732	14.841	8.681	5.770	2.787	2.589	24.782
no observations	no valid observations		-	1	1	1	10	8	41	671	10.330	32	1	38	2	39

b) Percentage of surface area [%]

	Recurrence interval (1984-2016)		Flooding probability	Jan	Feb	Mar	Apr	May	Jun	Jul	Aug	Sept	Oct	Nov	Dec	Annual
						erratic rains		Rainy season					erratic rains			
	no flooding observed		0%	98,71	98,75	98,59	99,04	98,04	99,09	97,48	85,60	95,01	96,70	98,38	98,52	85,80
water surface: rarely flooded or unreliable	$F_{<20}$	< once in 20yrs	<5%	0,02	0,02	0,07	0,01	0,02	0,00	0,02	0,01	0,16	0,17	0,24	0,18	10,52
	F_{10-20}	> once in 20yrs	5-10%	0,10	0,11	0,38	0,04	0,61	0,02	0,08	0,15	0,72	0,95	0,12	0,13	0,96
water surface: variably flooded	F_{5-10}	> once in 10yrs	10-20%	0,10	0,10	0,06	0,05	0,51	0,14	0,49	2,78	1,32	0,50	0,13	0,11	0,68
	F_{2-5}	> once in 5yrs	20-50%	0,15	0,14	0,08	0,09	0,14	0,12	0,83	3,94	1,28	0,62	0,17	0,13	0,97
	$F_{>2}$	> once in 2yrs	50%-90%	0,10	0,15	0,12	0,16	0,10	0,11	0,16	0,37	0,73	0,28	0,11	0,11	0,24
water surface: reliably flooded	F_0	every year	90%-100%	0,82	0,74	0,71	0,62	0,58	0,50	0,56	1,24	0,75	0,77	0,83	0,82	0,81
	flooded total		>0%	2.245	2.192	2.462	1.673	3.418	1.549	3.732	14.841	8.681	5.770	2.787	2.589	24.782
no observations	no valid observations		-	1	1	1	10	8	41	671	10.330	32	1	38	2	39

Table 6: Probability of flooding: Average monthly and annual surface water extent for water recurrence classes: a) average surface water extent, b) percentage of the study area.

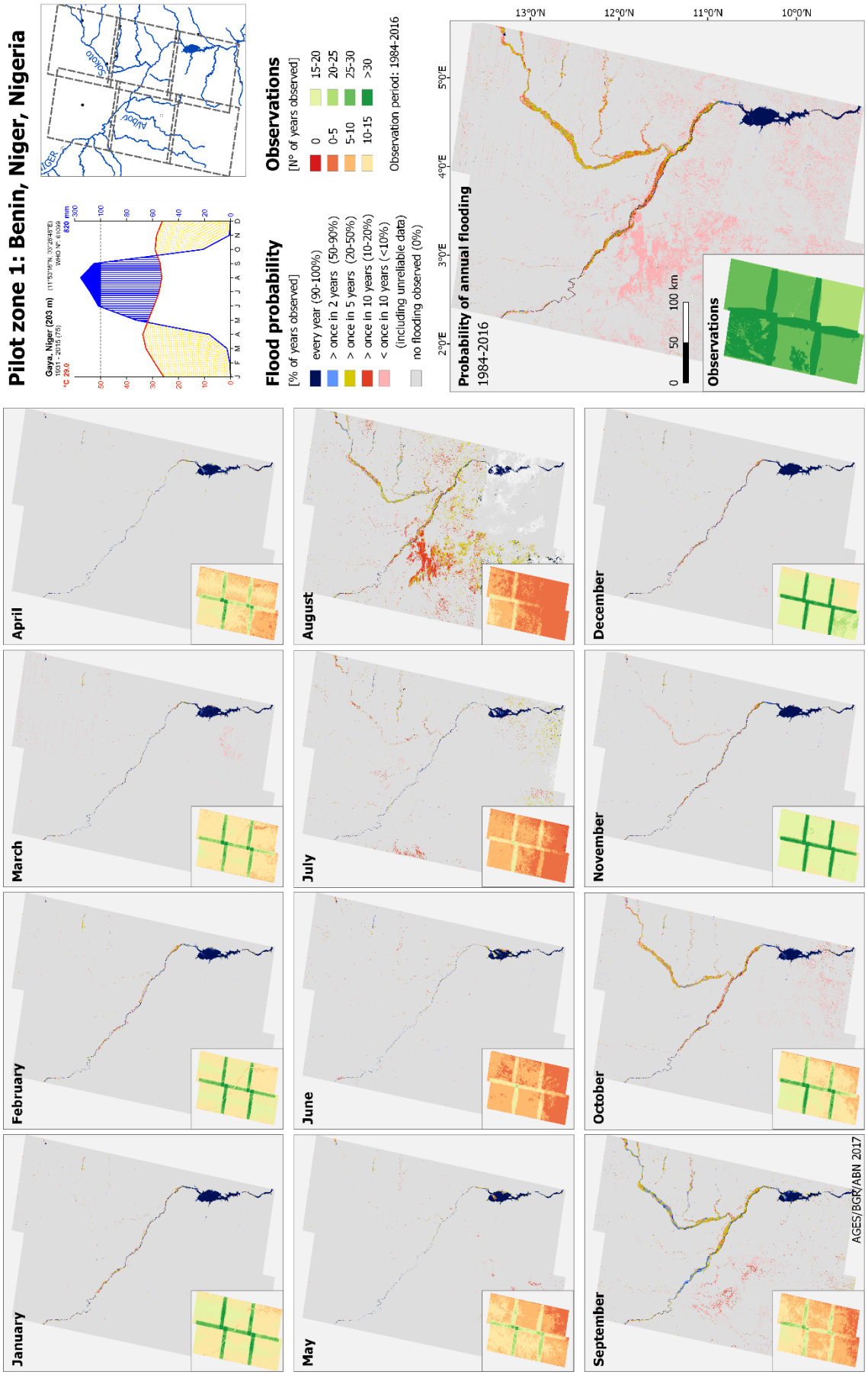

Figure 11: Probability of flooding and number of valid observations for the transboundary study area Benin-Niger-Nigeria. Observation period 1984 - 2016.

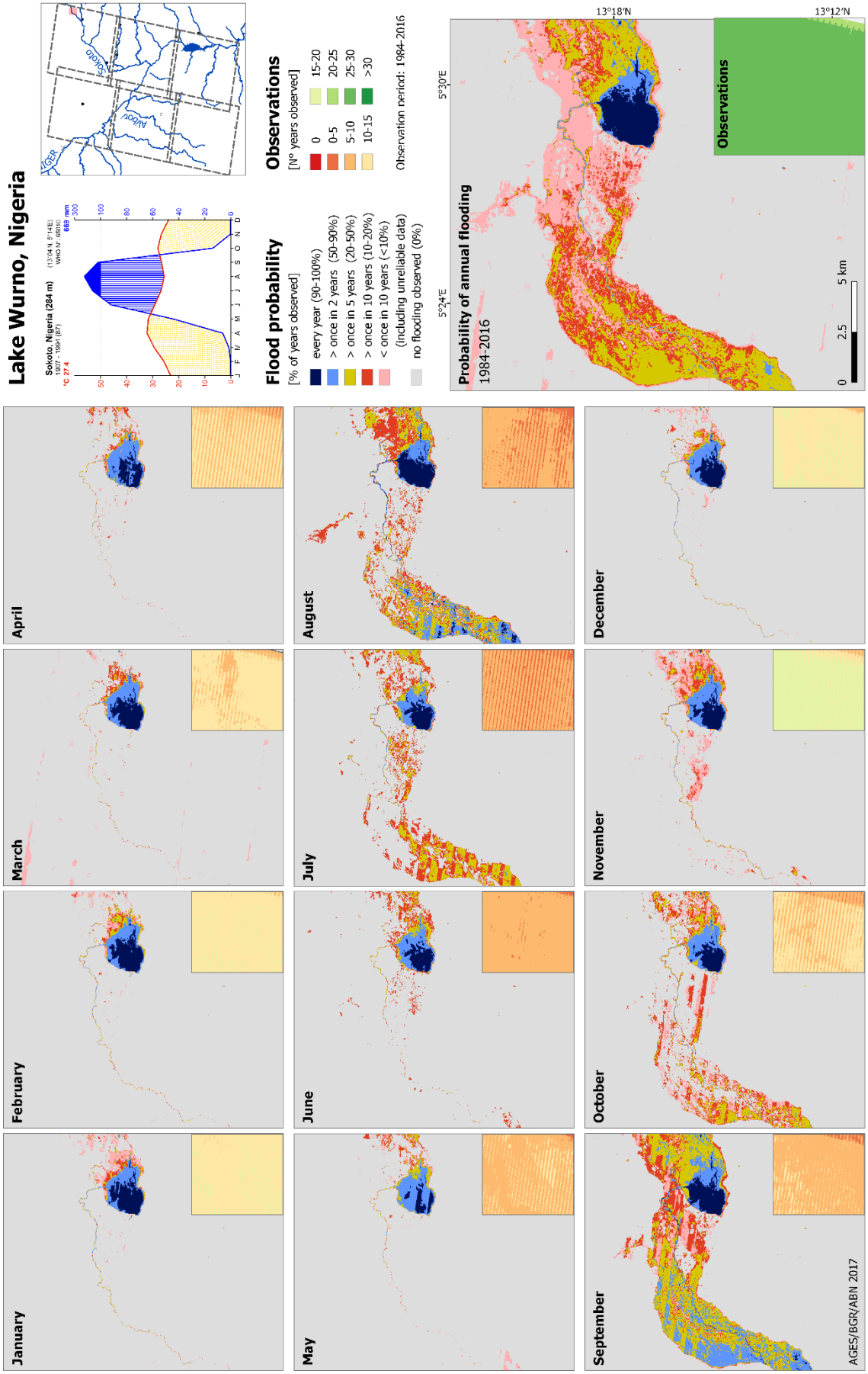

Figure 12: Probability of flooding and number of valid observations for the Lake Wurno, Nigeria. Observation period: 1984 - 2016.

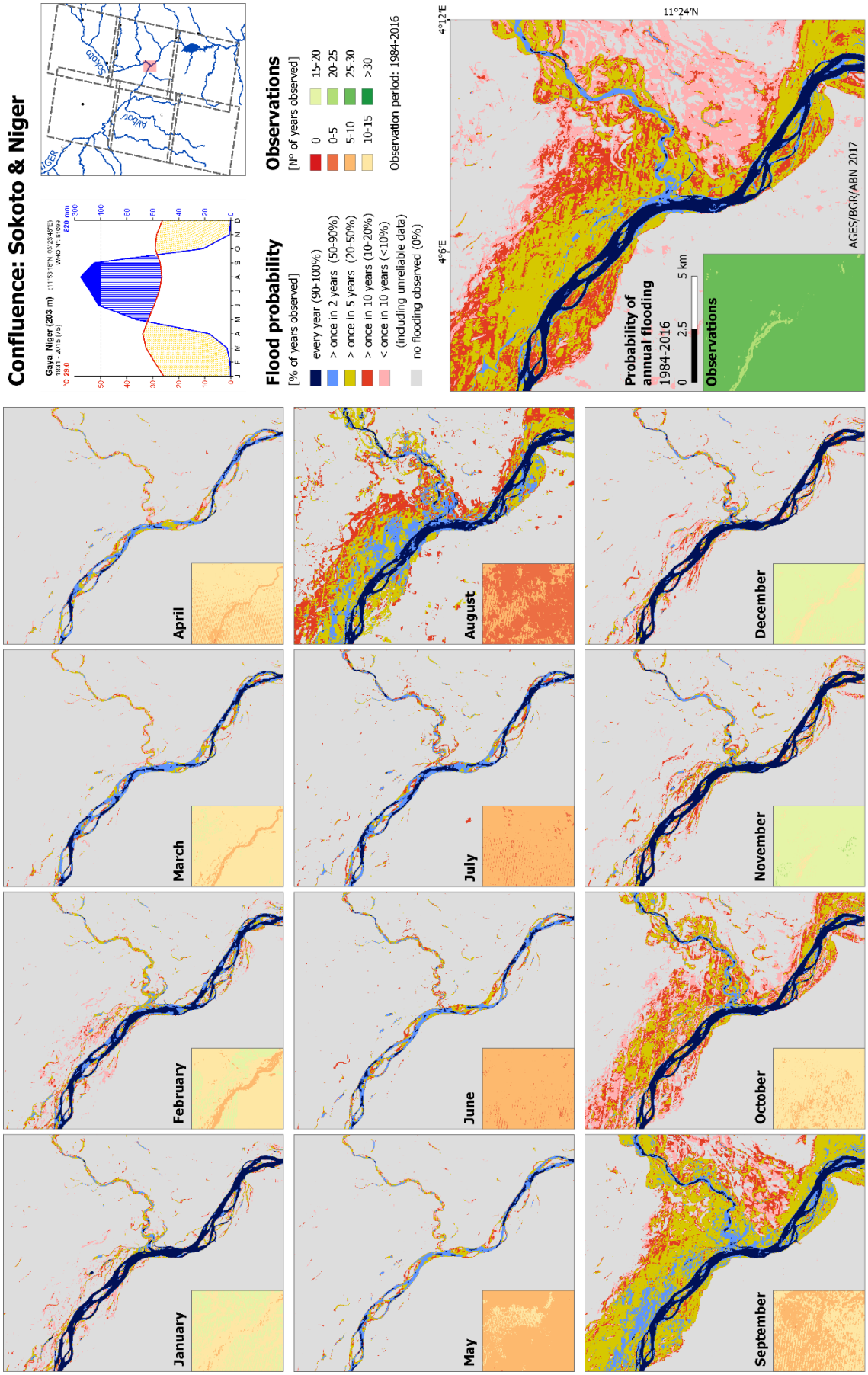

Figure 13: Probability of flooding and number of valid observations for the Sokoto—Niger confluence, Nigeria. Observation period 1984 - 2016.

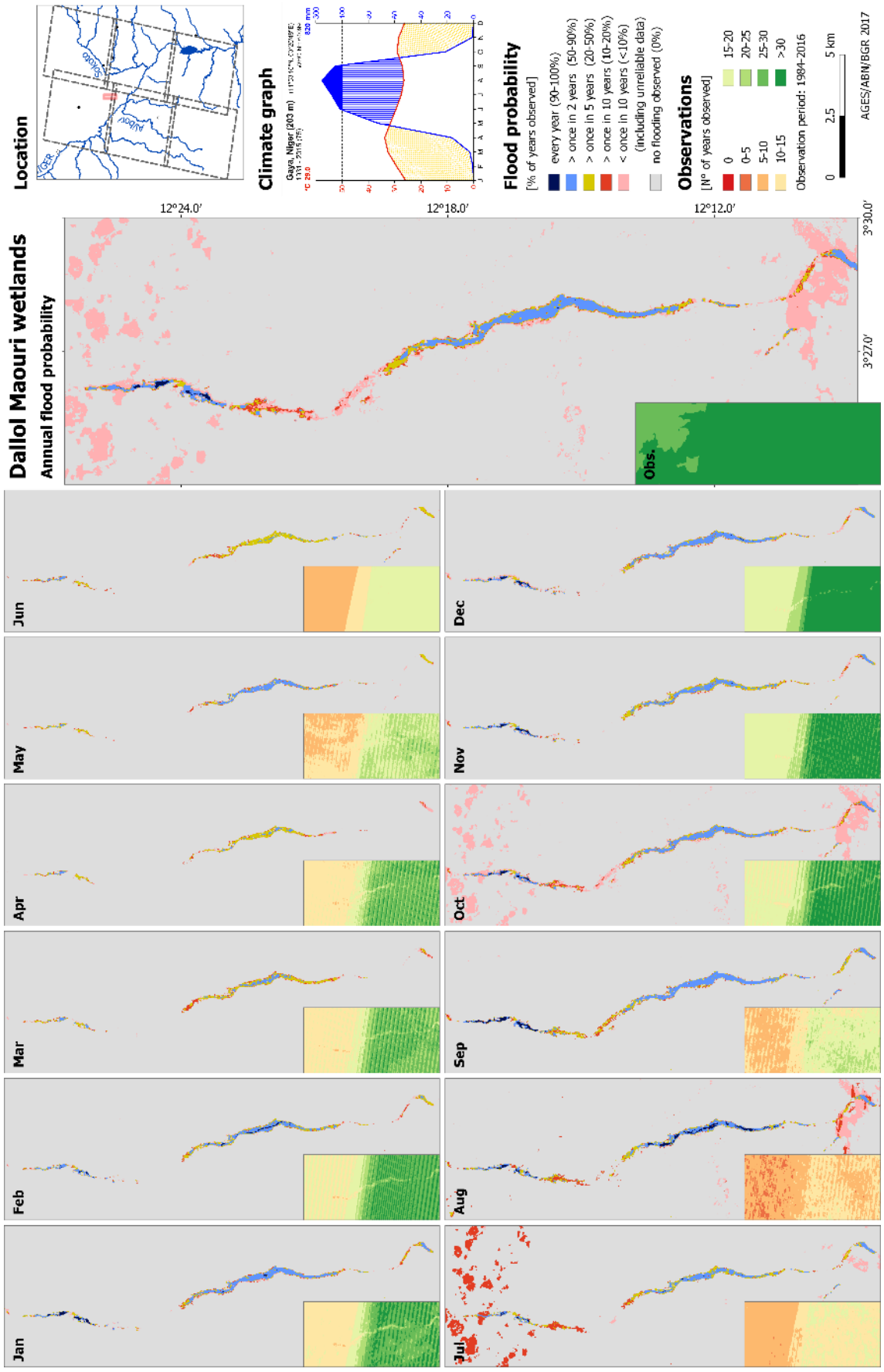

Figure 14: Probability of flooding and number of valid observations for the Dallol Maouri wetlands and salt lakes, Niger. Observation period 1984 - 2016.

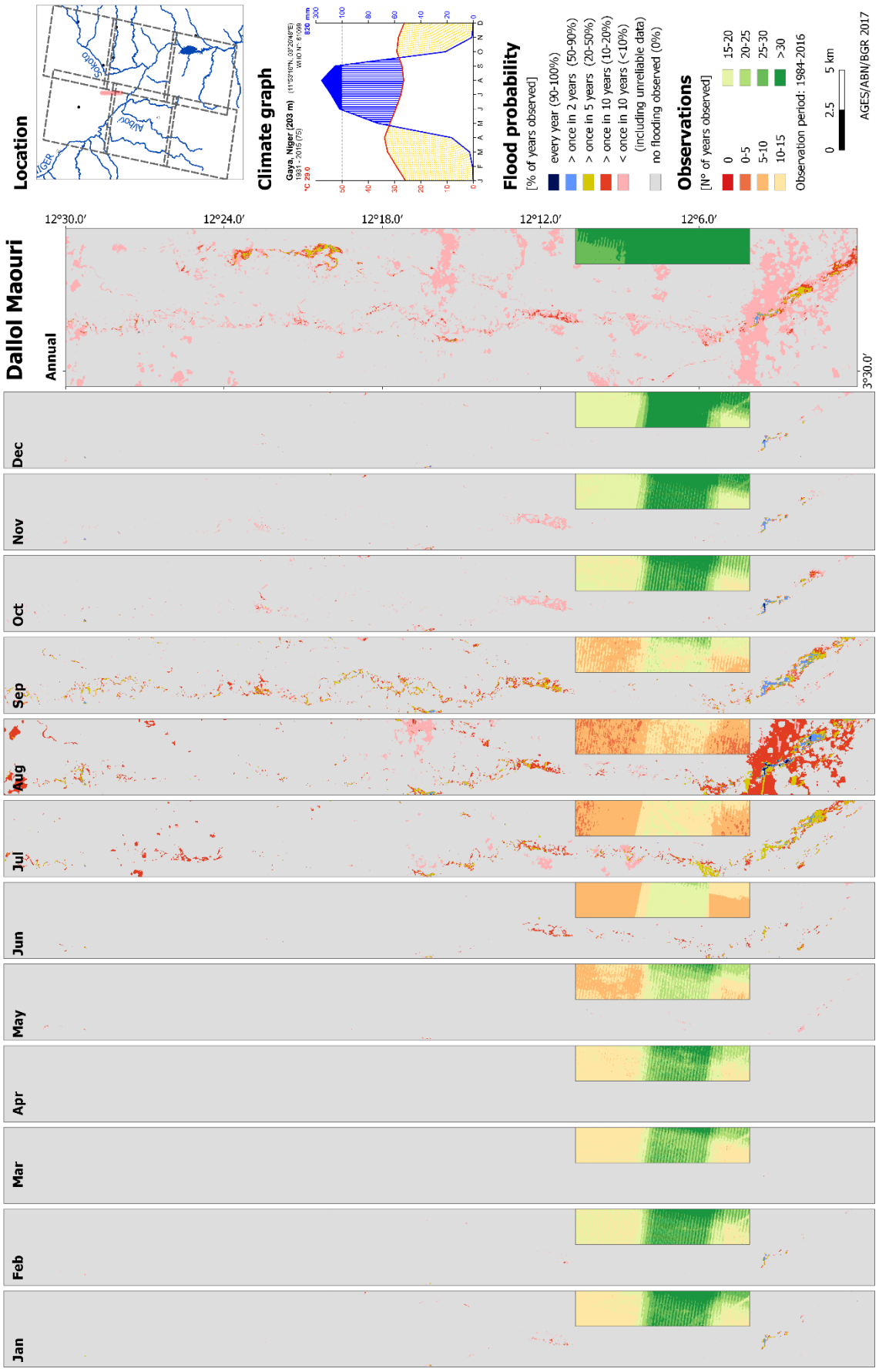

Figure 15: Probability of flooding and number of valid observations for the Dallol Maouri, Niger. Observation period 1984 - 2016.

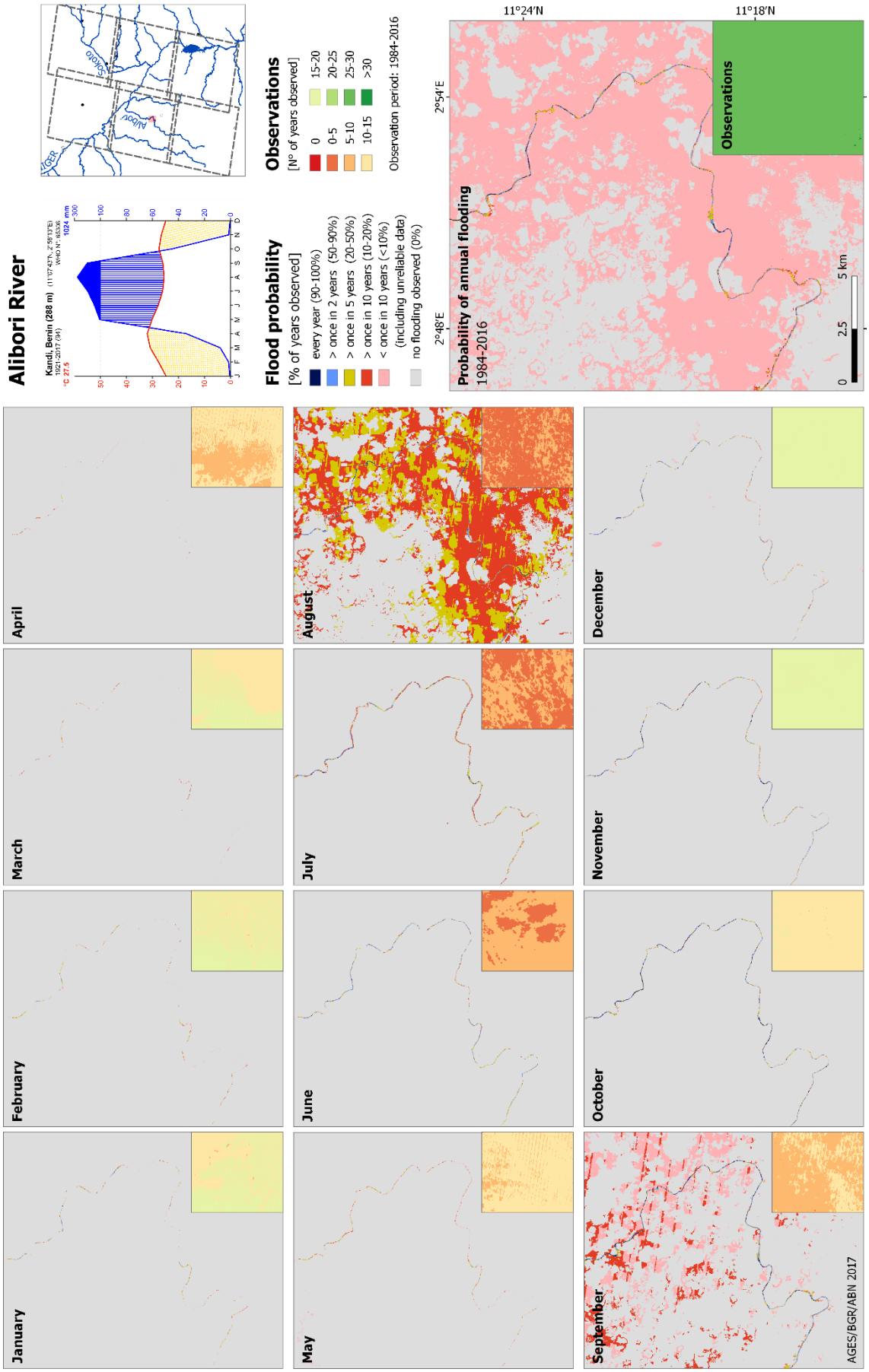

Figure 16: Probability of flooding and number of valid observations for the Alibori River, Benin. Observation period 1984 - 2016.

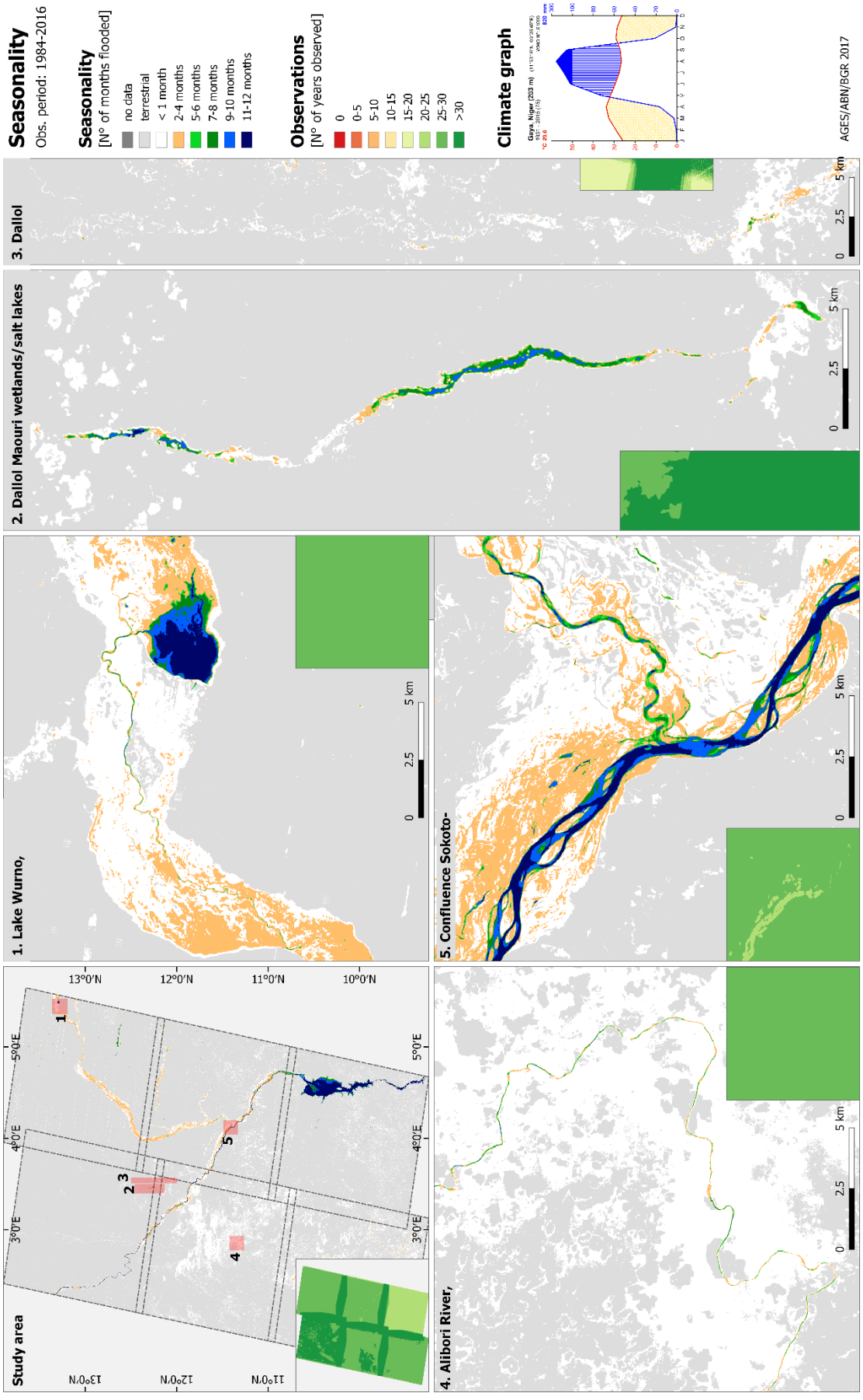

Figure 17: Seasonality of surface water for the study area and five zoom areas: Lake Wurno, Confluence Sokoto-Niger, Dallol Maouri, Dallol Maouri wetlands and the Alibori River. Observation period 1984 - 2016.

5.6 Surface water dynamics

Surface water dynamics in semi-arid areas show a high variability between years. Single years may deviate substantially from the mean and are not adequate to describe the hydrological system. Time series analysis provides **condensed and statistical averaged information** about the **general dynamics of surface water extent** and can provide a framework to evaluate observations of single years. Biased by the lack of observations, artefacts of the processing chain, and the inherent annual variability, interpretation of statistical summary parameters is limited to the main hydrological features.

Comparison of monthly surface water extent (Table 6, Figure 11 to Figure 16) with local **climate graphs** (Figure 1 and Figure 19) shows that flooding occurs towards the end of the rainy season between August and October. The earliest rains recorded by the climate stations in March and April are not reflected in the surface water record—except for (erratic) localized flood events. It is the strong precipitation increase in May and June that triggers the **onset of flooding occurring generally in July**. The minimum surface water extent as calculated here occurs, however, in June and July, well within the local rainy season reflecting a **time lag** of over two months between the initial erratic rains in April. The peak of the rainy season in August is responsible for major flooding and the concurrent maximum surface water extent. When rainfall ceases in September/October, flooding recedes rapidly. The reservoir function of the major river floodplains is reflected by another time lag observed between the maximum flooded area in August—concurrent with the local precipitation maximum—and the peak discharge measured at both the Alibori River and the Sokoto River in September (Figure 19).

5.6.1 Kandi basin

In Benin, the southern tributaries of the Niger (Mekrou/Pendjari, Alibori, and Sota) experience low water levels in April. Figure 16 shows the probability of monthly and annual flooding for an exemplary area along the Alibori River. With the arrival of the rains, streams fill slowly during May, June, and July reaching the maximum flooding extent in August. In September, river discharge is at its peak and floodplains along the valley bottoms are inundated. Yet in October, water levels of streams declined and by January, the Landsat images suggest that the perennial rivers draining the Kandi basin have virtually dried out. Due to their small size (the Mekrou is about 25 m wide at his confluence with the Niger) similar to the resolution of the Landsat images (30 m) and the mixed pixels effect, the MNDWI algorithm is not able to identify these rivers as permanent water bodies.

5.6.2 Sokoto basin

In Nigeria, flooding of the Sokoto River and its tributaries commences slowly with the incipient rains in May and June and inundation of the floodplain in July (Figure 12 & Figure 13). Maximum flooding of the plateau areas occurs in phase with peak precipitation in August, while floodplain inundation peaks in September. Surface water extents decrease rapidly in November, when the floodplain falls dry and in December, many seasonal streams have dried up. The seasonality parameters show that the Sokoto floodplain is flooded for a period of two, locally up to maximal four months (Figure 17). The headwaters of the Sokoto River stand out by ponds and numerous man-made reservoirs that retain the seasonal runoff for several months—but only the core areas of large reservoirs show a permanent water surface.

5.6.3 Southern Niger

The palaeodrainage channels in southern Niger—Dallol Maouri, Dallol Bosso, and Dallol Foga—show no perennial discharge and seasonal discharge is restricted to local flash floods rarely resulting in a continuous flow/discharge reaching the receiving Niger River. Lowest surface water extent is recorded for April (Figure 14 & Figure 15). Local inundations start in June, the first humid month recorded at the Gaya weather station. In July, extensive areas of the Dallol floodplains are inundated; the flooding

intensifies in August. In September, the flooding recedes. Locally, temporary and discontinuous drainage pathways develop.

Exceptions are permanent wetlands in depression locations of the palaeo-drainage system. Many of these are fed by locally artesian groundwater from the Continental Terminal 1 & 2 aquifers (FAO 1970; Guero 2003) but increase during the rainy season. The largest complex of "permanent saline/alkaline pools and seasonal streams and creeks" is located in the Middle Dallol Maouri (Ramsar Sites Information Service 2004). Its northern lake complex is reliable flooded each year and hosts permanent water bodies in its core area; the southern complex is flooded every other year (60 - 80 % of years observed). Large areas are nearly permanent lakes with a seasonality of 9 - 10 months (Figure 17).

5.6.4 Niger River floodplain

The water discharge of the Niger River is controlled by local rainfall triggering the "*crue rouge*" ("red flood", sometimes called "white flood") from July to October and the rainy season in its Guinean headwaters (Figure 18). The delayed arrival to the "*crue guinéene*" ("Guinean flood" or "black flood") maintains high water levels of the Niger River from November to April during the local dry season (Andersen et al. 2006; Descroix et al. 2012) but does not result in widespread flooding. Extensive inundation of the Niger floodplain only occurs during the local rainy season, particularly from August to October (Figure 11 & Figure 13).

With the onset of the rainy season in May (cf. Figure 1), localized flooding may occur anywhere. Only three months later in August, peak precipitation increases discharge and large areas of the floodplain become inundated. In August, persistent runoff from the tributaries leads to major ponding of the Niger floodplains lasting about three months from August to October—about a month longer than the rains. Surface water seasonality, indicates that the average duration of flooding of most of the floodplain areas ranges between two to three months per year.

In contrast to the declining flooding area (Figure 19), water levels of the Niger River continue on a high level until March/April of the following year. The "Guinean Flood" is fed by rainfall waters from the Upper Niger catchment in Guinea and Cote d'Ivoire.

While the "Guinean Flood" causes a strong rise and fall of water levels (Figure 18), the average extent of flooding along the Niger River as extracted here from the Landsat images remains similarly high throughout December to March with no indications for the peak of the "Guinean Flood". This is explained by a) comparably small areas of flooding within the riverbed corresponding to intermediate Niger River water levels, b) the high annual variability of the start, peak, and end of the "Guinean Flood" averaging the flooding signal of single years.

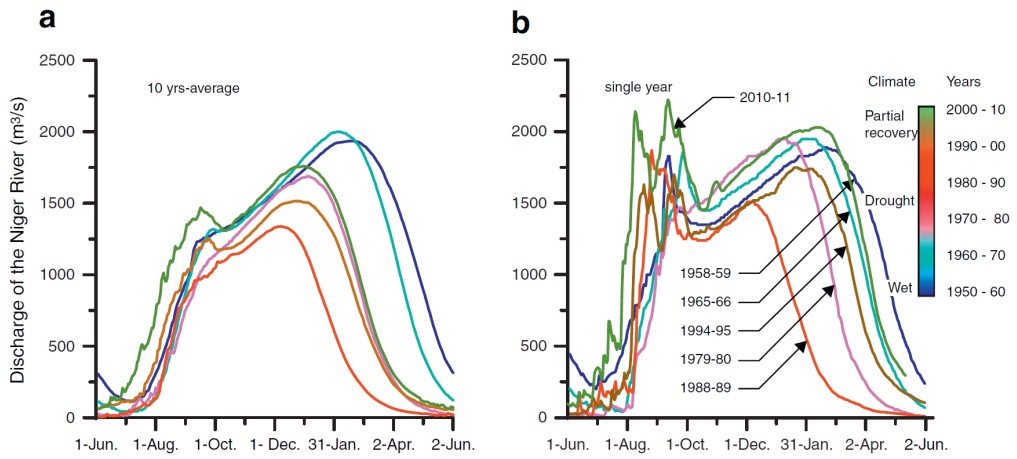

Figure 18: Hydrograph of the Niger River at Niamey a) mean decennial hydrograph b) individual hydrographs referring to the year with the earliest first flood in a given decade (from Descroix et al. 2012). Note the bimodal distribution reflecting the local "red flood" and the delayed "Guinean flood".

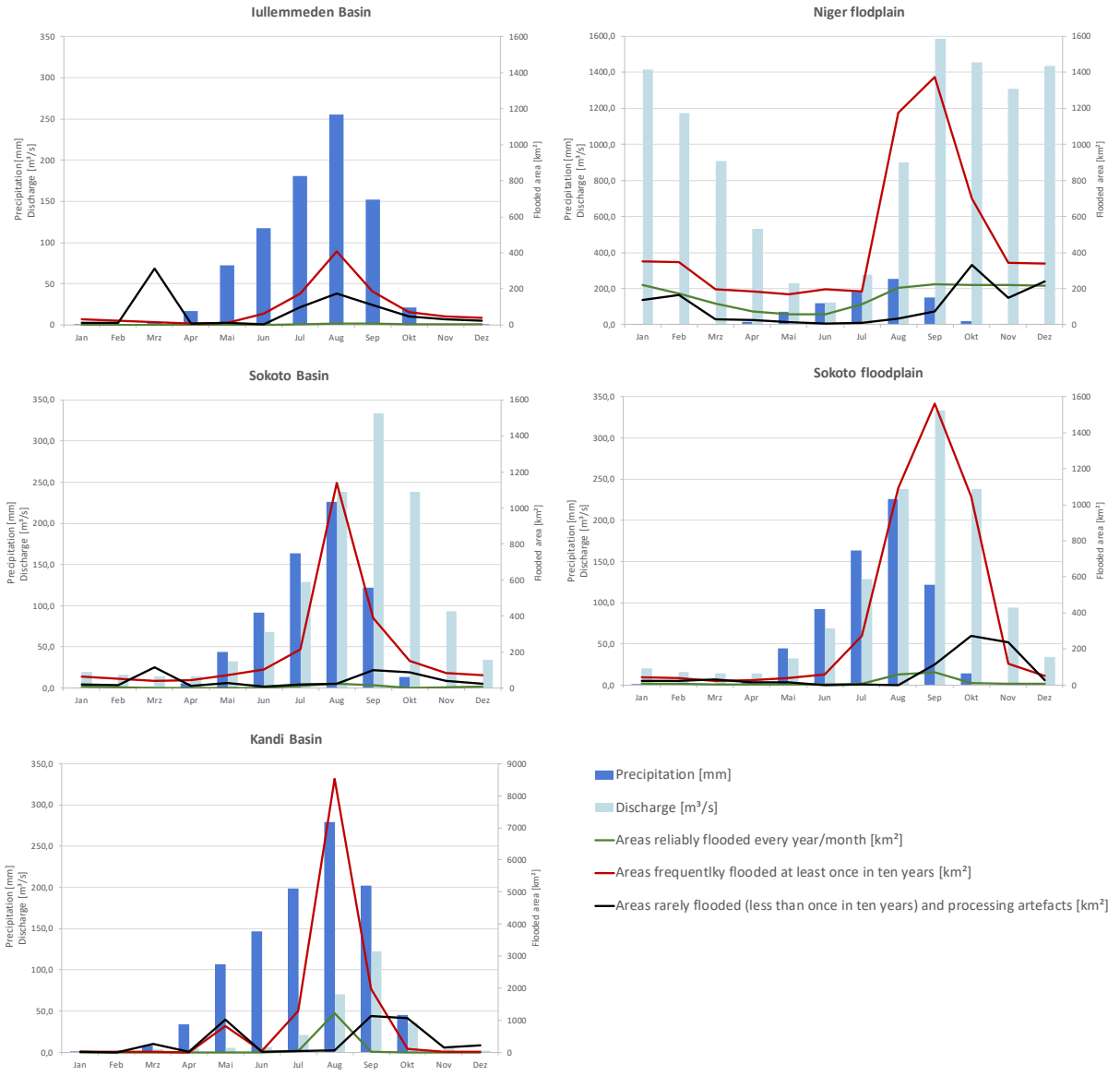

Figure 19: Comparison of local precipitation, discharge of the major local rivers, and flooded areas for five hydroecological zones: Iullemmeden Basin (meteorological station of Dosso, no local discharge measurements available), Niger floodplain (meteorological station of Gaya, discharge of the Niger River at Malanville), Sokoto Basin & floodplain (meteorological station of Sokoto, discharge of the Sokoto River at Kende), Kandi Basin (meteorological station of Kandi, discharge of the Alibori River at Yankin). Note the different scaling of the y-axes.

6 Limitations

6.1 Water extraction approach

Shortcomings of the surface water extent, the probability of flooding, and the seasonality arise from both the available data, the MNDWI algorithm, and the processing chain. While the time series approach offers statistical summaries of the flood extent, it is affected by the caveats of statistical abstraction.

Low numbers of valid observations in combination with poor quality data bias the validity and the explanatory power of the time series summary. Observations are restricted by:

- a low number of acquired Landsat scenes,
- a skewed seasonal and temporal distribution of scenes due to the Landsat acquisition plan,
- data gaps caused by the failure of the Landsat 7 ETM+ Scan Line Corrector (SLC-off),
- high cloud coverage

The low number of valid observations (often less than 12 observations per year) is one of the main limitations for the time series approach. The spatial and temporal coverage of the Landsat imagery is particularly critical during the rainy season—the main period of interest for the detection of flooding and temporal water body formation.

Misclassifications may arise from a low spectral separability between water and land, the chosen algorithm, or the available data, in particular the:

- discriminating power of the MNDWI algorithm and the chosen land-water threshold,
- radiometric saturation (chapter 4.3.1),
- spectral signature and a low separability by the chosen algorithm due to (among others):
    - a high plant water content,
    - the mixed pixel effect related to the similar size of water bodies (e.g. medium sized streams) and the resolution of the Landsat sensor (30 m).
- unsatisfactory USGS CFmask (cloud & SLC-off) and inclusion of distorted reflectance values

Both **overestimation** (e.g. high plant water content) and **underestimation** (e.g. mixed pixel effect, conservative MNDWI algorithm) do occur. High cloud cover limiting the number of observations may result in both over- and underestimation depending on the spatial distribution of the data gaps. In combination with misclassifications, the explanatory power of the statistical summary is strongly reduced and a positive bias is expected. The cloud mask provided by the USGS (CFmask) has shortcomings causing both omission and commission errors. Calculation of an own cloud mask, however, was far beyond the scope of this project. The MNDWI algorithm with a traditional zero threshold delineates a conservative minimum surface water extent (McFeeters 1996).

As a consequence, particularly the flooding class “Rarely flooded areas” with either a **seasonality of less than one month** or a **probability of flooding less than 10 %** (flooded less than once in 10 years, 11.5 % of the study area) should be regarded with caution and only provide a rough indication for flood–prone areas. Given low numbers of valid observations, single misclassifications may strongly bias any information from this large category.

The low temporal resolution and in particular the lack of observations during the rainy season **prevents the detection of short rainfall events**. The average estimates on a monthly basis can only be a minimum estimate.

6.2 USGS CFmask

The CFmask provided by the USGS is not a reliable tool to exclude clouds. Both commission and omission errors do occur on a large scale. Commission errors include the frequent classification of water bodies as clouds substantially reducing the number of valid observations. Visually not recognizable Cirrus clouds are one cause for such commission errors; however, the classification of linear water bodies as clouds suggests general shortcomings of the algorithm. On the other hand, transparent clouds often pass undetected and distort the reflectance signal, bias the number of valid observations, interfere with image enhancement techniques, and may result in an erroneous surface water classification.

The failure of the Landsat 7 Scan Line Corrector (SLC) in September 2003 caused data gaps with a typical stripe pattern. These so-called “SLC-off scenes” are included in this analysis to increase the number of observations. The CFmask was intended to mask the data gaps, however, often unsuccessfully. The prominent pattern of the SLC-off gaps visible in the surface water maps arise from a higher number of observations and are prone to misclassifications. Remote sensing approaches with access to the respective processing power and expertise suggest the development of adapted cloud masks and SLC-off mask. The here presented workflow is simplified and draws for convenience on the well-established USGS CFmask.

6.3 Plant water content

The spectral signature of green vegetation with a high plant water content may bias the detection of surface water using a spectral index such as MNDWI. The effect of plant water is observed for forest reserves in northern Benin and southern Nigeria, where open, agricultural areas border the last fragments of a natural Sudano-Sahelian dry savannah vegetation (Figure 16). Contribution of plant water to the spectral signal increases—spatially with increasingly semi-humid conditions and a moist savannah environment south of Kandi—and temporarily during the rainy season.

The MNDWI misclassifies areas with a high plant water contribution because of its fixed threshold and a low sensitivity to discriminate between water and land Misclassifications suspected to result from a high plant water content can be observed for the tiles Bembérèke (path 192/row 53), Kandi (path 192/row 52), and Kainji (path 191/row 53). In combination with a low number of valid observations, single misclassifications of vegetation as water may bias the calculated recurrence and seasonality values. The effect of plant water content on the MNDWI seems negligible in agricultural areas, the Sahelian dry savannah, and xeric scrublands of semi-arid Niger and northern Nigeria.

7 Applications

7.1 Urban planning, risk management, and disaster prevention

Flooding is a major hazard for human livelihoods. Flood management and prevention is essential for urban centres, villages, and agricultural areas to prevent human and economic loss. Based on information from the past 32 years (1984 - 2016), the flood probability estimates the average extent and the corresponding return periods of flood events. While the maximum flood extent (e.g. F_{10}) is not directly related to the corresponding peak flood discharge (e.g. Q_{10}), an analogue classification allows evaluating the hazard of flooding. The **flood probability map** delineates areas **vulnerable to flooding** that are inundated:

- regularly each year (F_0),
- at least every other year ($\approx F_2$),
- at least once in five years ($\approx F_5$), and
- less than once in ten years ($\approx F_{10}$).

The flood probability map provides local authorities, entrepreneurs, non-government organisation, and households with baseline information on the possible extent and the return period of inundation and highlights areas with a high vulnerability to flooding. Armed with information on the probability of flooding, urban development and infrastructure projects can be designed to reduce the vulnerability of settlements, industrial areas, and transportation towards the hazard of flooding

Local authorities can use the maps to:

- identify areas vulnerable to flooding,
- reduce the vulnerability to flooding of new infrastructure and urban development projects,
- elaborated flood management plans,
- identify evacuation routes and refugee sites,
- identify neuralgic spots of the embankment requiring protection or reinforcement,
- increase the public awareness of inundation hazards.

7.2 Groundwater recharge assessment

As the main source of drinking water in the Sahel region, groundwater is central for water security and agricultural and urban development. Recharge of the groundwater resource and replenishment of tapped aquifers occurs directly through the infiltration of precipitation or indirectly via the infiltration of surface waters.

Recharge areas of the aquifers in the Iullemmeden, Sokoto, and Kandi Basins are characterized by semi-arid and arid climates with low current rainfall and a low groundwater recharge. Particularly groundwater of deep aquifers with recharge areas in the Sahara desert might be (semi-)fossil dating back to the African Humid Period between ca. 15,000 and 5,000 years ago, when groundwater resources in the Sahara were replenished (Beyerle et al. 2003; Edmunds 2009). For the uppermost aquifers, isotope data and groundwater dating show a **partial recharge by local present-day precipitation**. Estimating the volume of contemporaneous groundwater recharge, however, remains a major challenge for sustainable groundwater management in the Sahel region (Edmunds et al. 2002; Favreau et al. 2009).

Recharge occurs via three major pathways. **Direct recharge** occurs via slow and diffuse infiltration of precipitation—a process most important in humid regions. In semi-arid environments, a considerable part of the groundwater recharge arises from **indirect, preferential flow** (Taylor et al. 2013; Jasechko & Taylor 2015). During strong and generally local rainfall events, water infiltrates

along zones of structural weakness bypassing the soil column. A third pathway is the gathering of surface runoff in geomorphic depressions or man-made retention pools facilitating infiltration through **indirect, localized infiltration**. Several studies from southern Niger suggest that indirect, depression-focused or localized groundwater recharge via the concentration of surface runoff in ponds is a major recharge source surpassing by far direct infiltration processes (Desconnets 1994; Massuel 2005; Favreau et al. 2009).

Maps of monthly flood probability and annual water seasonality provide a regional estimate of the spatial extent and the temporal variability of this localized recharge—baseline data for appraising the possible impact of such indirect recharge and to evaluating its potential relevance compared to other means of groundwater recharge. Indirect recharge below permanent water bodies is a static and spatially restricted process. The respective areas are the permanent water bodies as delineated by the water seasonality index. Indirect, depression-focused recharge is dynamic and particularly important in areas of seasonal flooding. In the study area, ponding and flooding are in general related to the local rains and can be mapped either by the seasonality index delineating areas flooded less than 4 months or by the monthly water recurrence index for the rainy period, comprising generally the months July to October.

The temporal resolution–on average a fortnightly flyover of the Landsat satellites—and the low number of observations caused by cloud cover during the rainy season only permit summary statistics for time slices of one month (see chapter 5.3—probability of monthly flooding). Based on the data availability, detection of such localized recharge processes is restricted to major and lasting events with durations exceeding one (1) month (see chapter 5.4—seasonality). Short-term flooding due to single rainfall events or flash floods cannot be accounted for and the **extent and frequency of seasonal ponding is underestimated**.

Remote sensing offers a **rough estimation of areas relevant for groundwater recharge**. For a more detailed analysis, local hydrogeological conditions have to be taken into account; for example the hydraulic connection between surface water bodies and the groundwater resource. Hydrogeological research has shown, that the Niger River as well as the lower reaches of the Dallol Maouri, the Sokoto River, and the Sota River are **groundwater discharge areas**. Here, flooding does not result in groundwater recharge but contrarily may indicate enhance groundwater discharge.

8 References

Andersen, I, Dione, O, Jarosewich-Holder, M, Olivry, J-C, George Golitzen, K & International Bank for Reconstruction and Development (eds) (2006): *Le Bassin du fleuve Niger: vers une vision de développement durable*. Directions in development, Banque Mondiale, Washington, DC.

Bertram, A, Wendleder, A, Schmitt, A & Huber, M (2016): Long-term monitoring of water dynamics in the Sahel region using the Multi-SAR System.

Beyerle, U, Rueedi, J, Leuenberger, M, Aeschbach-Hertig, W, Peeters, F, Kipfer, R & Dodo, A (2003): Evidence for periods of wetter and cooler climate in the Sahel between 6 and 40 kyr BP derived from groundwater. *Geophysical Research Letters*, vol. 30, no. 4 p. n/a-n/a.

Boschetti, M, Nutini, F, Manfron, G, Brivio, PA & Nelson, A (2014): Comparative Analysis of Normalised Difference Spectral Indices Derived from MODIS for Detecting Surface Water in Flooded Rice Cropping Systems. *PLoS ONE*, vol. 9, no. 2.

Carroll, ML, Townshend, JR, DiMiceli, CM, Noojipady, P & Sohlberg, RA (2009): A new global raster water mask at 250 m resolution. *International Journal of Digital Earth*, vol. 2, no. 4 pp. 291–308.

Desconnets, J-C (1994): Typologie et caractérisation hydrologique des systèmes endoréiques en milieu sahélien (Niger - degré carré de Niamey). Doctoral thesis thesis, Université de Montpellier II, Montpellier.

Descroix, L, Genthon, P, Amogu, O, Rajot, J-L, Sighomnou, D & Vauclin, M (2012): Change in Sahelian Rivers hydrograph: The case of recent red floods of the Niger River in the Niamey region. *Global and Planetary Change*, vol. 98–99 pp. 18–30.

Donchyts, G, Baart, F, Winsemius, H, Gorelick, N, Kwadijk, J & van de Giesen, N (2016a): Earth's surface water change over the past 30 years. *Nature Climate Change*, vol. 6, no. 9 pp. 810–813.

Donchyts, G, Schellekens, J, Winsemius, H, Eisemann, E & van de Giesen, N (2016b): A 30 m Resolution Surface Water Mask Including Estimation of Positional and Thematic Differences Using Landsat 8, SRTM and OpenStreetMap: A Case Study in the Murray-Darling Basin, Australia. *Remote Sensing*, vol. 8, no. 5 p. 386.

Du, Y, Zhang, Y, Ling, F, Wang, Q, Li, W & Li, X (2016): Water Bodies' Mapping from Sentinel-2 Imagery with Modified Normalized Difference Water Index at 10-m Spatial Resolution Produced by Sharpening the SWIR Band. *Remote Sensing*, vol. 8, no. 4 p. 354.

Edmunds, W, Fellman, E, Goni, I & Prudhomme, C (2002): Spatial and temporal distribution of groundwater recharge in northern Nigeria. *Hydrogeology Journal*, vol. 10, no. 1 pp. 205–215.

Edmunds, WM (2009): Palaeoclimate and groundwater evolution in Africa—implications for adaptation and management. *Hydrological Sciences Journal*, vol. 54, no. 4 pp. 781–792.

FAO (1970): *Etudes en vue de la mise en valeur du Dallol Maouri. Niger: Les eaux souterraines*. vol 1, Rapport technique, FAO/UNDP, Rome.

Favreau, G, Cappelaere, B, Massuel, S, Leblanc, M, Boucher, M, Boulain, N & Leduc, C (2009): Land clearing, climate variability, and water resources increase in semiarid southwest Niger: A review. *Water Resources Research*, vol. 45.

Feng, M, Sexton, JO, Channan, S & Townshend, JR (2016): A global, high-resolution (30-m) inland water body dataset for 2000: first results of a topographic–spectral classification algorithm. *International Journal of Digital Earth*, vol. 9, no. 2 pp. 113–133.

Feyisa, GL, Meilby, H, Fensholt, R & Proud, SR (2014): Automated Water Extraction Index: A new technique for surface water mapping using Landsat imagery. *Remote Sensing of Environment*, vol. 140 pp. 23–35.

Gao, H, Wang, L, Jing, L & Xu, J (2016): An effective modified water extraction method for Landsat-8 OLI imagery of mountainous plateau regions. *IOP Conference Series: Earth and Environmental Science*, vol. 34 p. 012010.

Guero, A (2003): Etude des relations hydrauliques entre les différentes nappes du complexe sédimentaire de la bordure sud-ouest du bassin des Iullemeden (Niger) - Approches géochimiques et hydrodynamiques. Dissertation thesis, Université Paris XI, Orsay.

Hansen, MC, Potapov, PV, Moore, R, Hancher, M, Turubanova, SA, Tyukavina, A, Thau, D, Stehman, SV, Goetz, SJ, Loveland, TR, Kommareddy, A, Egorov, A, Chini, L, Justice, CO & Townshend, JRG (2013): High-Resolution Global Maps of 21st-Century Forest Cover Change. *Science*, vol. 342, no. 6160 pp. 850–853.

Jasechko, S & Taylor, RG (2015): Intensive rainfall recharges tropical groundwaters. *Environmental Research Letters*, vol. 10, no. 12 p. 124015.

Ju, J & Roy, DP (2008): The availability of cloud-free Landsat ETM+ data over the conterminous United States and globally. *Remote Sensing of Environment*, vol. 112, no. 3 pp. 1196–1211.

Jung, HC, Alsdorf, D, Moritz, M, Lee, H & Vassolo, S (2011): Analysis of the relationship between flooding area and water height in the Logone floodplain. *Physics and Chemistry of the Earth, Parts A/B/C*, vol. 36, no. 7–8 pp. 232–240.

Klein, I, Dietz, A, Gessner, U, Dech, S & Kuenzer, C (2015a): Results of the Global WaterPack: a novel product to assess inland water body dynamics on a daily basis. *Remote Sensing Letters*.

Klein, I, Dietz, AJ, Gessner, U & Kuenzer, C (2015b): Global WaterPack: Intra-annual Assessment of Spatio-Temporal Variability of Inland Water Bodies. in C Kuenzer, S Dech & W Wagner (eds), *Remote Sensing Time Series*, Remote Sensing and Digital Image Processing, Springer International Publishing pp. 99–117.

Klein, I, Gessner, U, Dietz, AJ & Kuenzer, C (2017): Global WaterPack – A 250m resolution dataset revealing the daily dynamics of global inland water bodies. *Remote Sensing of Environment*, vol. 198 pp. 345–362.

Kovalskyy, V & Roy, DP (2013): The global availability of Landsat 5 TM and Landsat 7 ETM+ land surface observations and implications for global 30m Landsat data product generation. *Remote Sensing of Environment*, vol. 130 pp. 280–293.

Lamarche, C, Santoro, M, Bontemps, S, d'Andrimont, R, Radoux, J, Giustarini, L, Brockmann, C, Wevers, J, Defourny, P & Arino, O (2017): Compilation and Validation of SAR and Optical Data Products for a Complete and Global Map of Inland/Ocean Water Tailored to the Climate Modeling Community. *Remote Sensing*, vol. 9, no. 1 p. 36.

Lehner, B & Döll, P (2004): Development and validation of a global database of lakes, reservoirs and wetlands. *Journal of Hydrology*, vol. 296, no. 1–4 pp. 1–22.

Lehner, B, Verdin, K & Jarvis, A (2008): New Global Hydrography Derived From Spaceborne Elevation Data. *Eos, Transactions American Geophysical Union*, vol. 89, no. 10 pp. 93–94.

Lillesand, T, Kiefer, RW & Chipman, J (2015): *Remote Sensing and Image Interpretation*. 7th edn, John Wiley & Sons, Hoboken, N.J.

Liu, Z, Yao, Z & Wang, R (2016): Assessing methods of identifying open water bodies using Landsat 8 OLI imagery. *Environmental Earth Sciences*, vol. 75, no. 10 p. 873.

Massuel, S (2005): Evolution récente de la ressource en eau consécutive aux changements climatiques et environnementaux du sud-ouest Niger. Modélisation des eaux de surface et souterraines du bassin du kori de Dantiandou sur la période 1992-2003. phdthesis thesis, Université Montpellier II - Sciences et Techniques du Languedoc.

McFeeters, SK (1996): The use of the Normalized Difference Water Index (NDWI) in the delineation of open water features. *International Journal of Remote Sensing*, vol. 17, no. 7 pp. 1425–1432.

Messager, ML, Lehner, B, Grill, G, Nedeva, I & Schmitt, O (2016): Estimating the volume and age of water stored in global lakes using a geo-statistical approach. *Nature Communications*, vol. 7 p. 13603.

Moser, L, Schmitt, A & Wendleder, A (2016): Automated Wetland Delineation from Multi-Frequency and Multi-Polarized SAR Images in High Temporal and Spatial Resolution. *ISPRS Annals of Photogrammetry, Remote Sensing and Spatial Information Sciences* pp. 57–64.

Mueller, N, Lewis, A, Roberts, D, Ring, S, Melrose, R, Sixsmith, J, Lymburner, L, McIntyre, A, Tan, P, Curnow, S & Ip, A (2016): Water observations from space: Mapping surface water from 25 years of Landsat imagery across Australia. *Remote Sensing of Environment*, vol. 174 pp. 341–352.

Pekel, J-F, Cottam, A, Gorelick, N & Belward, AS (2016): High-resolution mapping of global surface water and its long-term changes. *Nature*, vol. 540, no. 7633 pp. 418–422.

Ramsar Sites Information Service (2004): *Dallol Maouri: Ramsar Sites Information Service, Site N° 1381*. accessed 19.09.2017, <https://rsis.ramsar.org/ris/1381>.

Rogers, AS & Kearney, MS (2004): Reducing signature variability in unmixing coastal marsh Thematic Mapper scenes using spectral indices. *International Journal of Remote Sensing*, vol. 25, no. 12 pp. 2317–2335.

Rouse, JW (1974): *Monitoring the vernal advancement and retrogradation (green wave effect) of natural vegetation*.

Roy, DP, Ju, J, Mbow, C, Frost, P & Loveland, T (2010): Accessing free Landsat data via the Internet: Africa's challenge. *Remote Sensing Letters*, vol. 1, no. 2 pp. 111–117.

Shen, L & Li, C (2010): Water body extraction from Landsat ETM+ imagery using adaboost algorithm. in *2010 18th International Conference on Geoinformatics* pp. 1–4.

Sheng, Y, Song, C, Wang, J, Lyons, EA, Knox, BR, Cox, JS & Gao, F (2016): Representative lake water extent mapping at continental scales using multi-temporal Landsat-8 imagery. *Remote Sensing of Environment*, vol. 185 pp. 129–141.

Taylor, RG, Todd, MC, Kongola, L, Maurice, L, Nahozya, E, Sanga, H & MacDonald, AM (2013): Evidence of the dependence of groundwater resources on extreme rainfall in East Africa. *Nature Climate Change*, vol. 3, no. 4 pp. 374–378.

Tulbure, M (2015): Spatiotemporal Dynamics of Surface Water Extent from Three Decades of Seasonally Continuous Landsat Time Series at Subcontinental Scale. in *2015 AGU Fall Meeting*, Agu.

Tulbure, MG & Broich, M (2013): Spatiotemporal dynamic of surface water bodies using Landsat time-series data from 1999 to 2011. *ISPRS Journal of Photogrammetry and Remote Sensing*, vol. 79 pp. 44–52.

US Geological Survey (2000): *HYDRO 1k Elevation Derivative Database*. Earth Resources Observation and Science (EROS) Data Center (EDC), Sioux Falls.

USGS (2016a): *Landsat 4-7 Climate Data Record (CDR) Surface Reflectance*. Product Guide N°Version 6.7, August 2016, USGS p. 27.

USGS (2016b): *Provisional Landsat 8 Surface Reflectance Code (LaSRC) Product*. Product Guide N°Version 3.1, August 2016, USGS p. 27.

Verpoorter, C, Kutser, T, Seekell, DA & Tranvik, LJ (2014): A global inventory of lakes based on high-resolution satellite imagery. *Geophysical Research Letters*, vol. 41, no. 18 p. 2014GL060641.

Westra, T & De Wulf, RR (2009): Modelling yearly flooding extent of the Waza-Logone floodplain in northern Cameroon based on MODIS and rainfall data. *International Journal of Remote Sensing*, vol. 30, no. 21 pp. 5527–5548.

Wilczok, C (2014): *Compilation of the yearly flooding extent opf the Waza-Logone floodplain based on MODIS time series 2000-2013*. Technical Report, Lake Chad Basin: Sustainable Water Management N°9, BGR, Hanover p. 19.

Wilson, EH & Sader, SA (2002): Detection of forest harvest type using multiple dates of Landsat TM imagery. *Remote Sensing of Environment*, vol. 80, no. 3 pp. 385–396.

Wulder, MA, White, JC, Loveland, TR, Woodcock, CE, Belward, AS, Cohen, WB, Fosnight, EA, Shaw, J, Masek, JG & Roy, DP (2016): The global Landsat archive: Status, consolidation, and direction. *Remote Sensing of Environment*, vol. 185 pp. 271–283.

Xu, H (2006): Modification of normalised difference water index (NDWI) to enhance open water features in remotely sensed imagery. *International Journal of Remote Sensing*, vol. 27, no. 14 pp. 3025–3033.

Yamazaki, D, Trigg, MA & Ikeshima, D (2015): Development of a global ~90m water body map using multi-temporal Landsat images. *Remote Sensing of Environment*, vol. 171, no. Supplement C pp. 337–351.

Yang, K, Li, M, Liu, Y, Cheng, L, Duan, Y & Zhou, M (2014): River Delineation from Remotely Sensed Imagery Using a Multi-Scale Classification Approach. *IEEE Journal of Selected Topics in Applied Earth Observations and Remote Sensing*, vol. 7, no. 12 pp. 4726–4737.

9 Appendix

9.1 Digital water masks and stream networks

Digital baseline data on stream networks, lakes, and water bodies in different scales and detail is available. The datasets differ by data format (raster or vector data), data sources, and the period targeted. The adequate choice of a water mask or a stream network depend on the data format—raster or vector data—the required spatial resolution, comprehensiveness, accuracy, and added information such as ecological classification or seasonality (Table 7). The following paragraphs present a selection of nine different global water body or stream network data sets (status as of 2017) classed according to the three main data sources for stream networks and water bodies: topographic maps, digital elevation models, and remote sensing.

9.1.1 Topographic maps

The first category of digital stream networks was extracted (manually) from topographic maps and resulted in the Digital Chart of the World (DCW, 1993)—also called Smart Vector Map (VMap)—or the Global Lakes and Wetland Database (GLWD, 2004). These digital databases provide a variety of thematic information; the stream network being one of many.

Digital Chart of the World (DCW) and Vector Map (VMap)

The first freely available, globally comprehensive, geographic digital data set was the **Digital Chart of the World (DCW**) and its successor the **Vector (Smart) Map (VMap).** The DCW is a 1:1,000,000 scale vector base map produced by the National Imagery and Mapping Agency (NIMA) and ESRI and designed for aeronautical use. The last documented update was 1992. It is freely available since 2006. The DCW is a comprehensive GIS and includes topography, hydrography, infrastructure, census data, and place names. The primary source of this database is the 1:1,000,000 scale Operational Navigation Chart (ONC) map series produced by the military mapping authorities of USA, UK, Australia, and Canada. Recent DCW and VMap downloads often claim to be updated DCW databases. The updates, however, lack reliable information when an update has taken place, and which entity is responsible for the improvements.

The Vector Map level 0 (VMap0) provides the recent DCW on a small scale (1:1,000,000). Medium (VMap1, 1:250,000) and high-resolution (VMap2) levels comprise higher resolution data for selected countries only. Access is via unofficial webpages such as mapability (http://www.mapability.com/index1.html) or GISLab (http://gis-lab.info/qa/vmap0-eng.html) and other open data websites.

Global Lakes and Wetland Database (GLWD)

The Global Lakes and Wetlands Database (Lehner & Döll 2004) has been compiled from a variety of sources, mainly collections of pre-existing maps. Global data on lakes and wetlands is available at three levels. Vector data at level 1 consists of major lakes and reservoirs only; level 2 includes water bodies with a surface area => 0.1 km², excluding level 1 data. Level 3 data is a comprehensive, 30 sec raster dataset differentiating 12 classes of different types of lakes and wetlands. Access to the database and documentation are provided via the WWF (https://www.worldwildlife.org/pages/global-lakes-and-wetlands-database).

9.1.2 Digital elevation models

Since 2000, remote sensing techniques have been applied to identify water bodies from space. Based on the SRTM digital elevation model, several water masks were produced such as the SRTM Water Body Data (SWDB) and the HydroSHEDS data set family (Lehner et al. 2008). The high-resolution digital elevation data of the Shuttle Mission (3 arc-second, ≈ 90 m) and 1 arc-second (≈ 30 m)) allowed delineation of potential drainage networks as defined by the topography in February 2000. HydroSHEDS provide a globally consistent and hydrological sound drainage network on a 15 arc-second scale. Actual watercourses differ from these relief-determined potential drainage networks, particularly in arid areas. Despite its potentially higher resolution of 1 arc-second, the SWDB outlines only large, water bodies that have been verified using pre-existing data such as the GLWD, maps and others. The SWDB does not provide a detailed stream network.

HYDRO1K

HYDRO1K provides hydrologic baseline data on a continent-scale (US Geological Survey 2000). It was developed from the USGS EROS Center and is derived from the 30 arc-second (1 km) digital elevation model of the world (GTOPO30, 1996) produced by the USGS from a variety of topographic maps, digital elevation data and vector sources e.g. the digital chart of the world (DCW). Hydro1K is a globally consistent hydrologic derivative data set consisting of a hydrologically correct DEM, flow directions, flow accumulation, slope, aspect , compound (wetness) index as well as vector data of streamlines and basins. The main limitation is the low spatial resolution. Hydro1K can be accessed via https://earthexplorer.usgs.gov/.

Documentation can be found at https://www.usgs.gov/centers/eros/science/usgs-eros-archive-digital-elevation-hydro1k.

SRTM Water Body Data (SWDB) (2003)

The SRTM Water Body Data (SWBD) is a high-resolution (30 m) vector dataset. Shorelines of oceans, lakes, rivers with extents exceeding an area of 600 m in length and 183 m in width, and inlets greater than 90 m were delineated and depicted as water bodies. The data set was created by the US National Geospatial-Intelligence Agency (NGA) as a by-product of the digital elevation model of the Shuttle Radar Topography Mission (SRTM) Digital Terrain Elevation Data Level 2 (DTED®2) with a resolution of 1 arc-second (approx.. 30 m).

Water bodies are outlined as of February 2000. Voids are filled with land cover data from Landsat 5, dating a decade earlier. SRTM data can be downloaded via Earth Explorer https://earthexplorer.usgs.gov/. Documentation is available at

https://www.usgs.gov/centers/eros/science/usgs-eros-archive-digital-elevation-shuttle-radar-topography-mission-water-body

HydroSHEDS & HydroLAKES

HydroSHEDS (Hydrological data and maps based on SHuttle Elevation Derivatives at multiple Scales) provides consistent hydrographic information on a global scale (Lehner et al. 2008). HydroSHEDS are derived from the digital elevation data of the Shuttle Radar Topography Mission (SRTM) at 3 arc-second resolution (≈ 90 m). Auxiliary data has been incorporated from the SRTM Water Body Data SWDB, the Global Lakes and Wetlands Database (GLWD), the Digital Chart of the World (DCW) and others. HydroSHEDS comprises a hydrologically-conditioned elevation model, a void-filled digital elevation model, and hydrological derivates such as flow accumulation and flow direction. River network and major drainage basins are available as vector data.

Elevation datasets are available with resolutions of 3 arc-second (approx. 90 meters at the equator), 15 arc-second, or 30 arc-second resolutions with a seamless near-global extent. Stream networks only at 15 and 30 arc-second resolution. Being based on the Shuttle Radar Topographic Mission, the elevation information dates to February 2000. HydroSHEDS has been developed by the Conservation Science Program of the World Wildlife Fund (WWF) in collaboration with the U.S. Geological Survey (USGS) and other research institutes (http://www.hydrosheds.org/ & https://hydrosheds.cr.usgs.gov/).

In 2016, HydroLAKES was introduced as a database of about 1.4 Mio lakes with a surface area of at least 10 ha. It provides shoreline polygons but also parameters such as residence time and lake depth (Messager et al. 2016).

9.1.3 Remote sensing

Direct delineation of water became possible using optical sensors such as Landsat sensor family (1972, ongoing), MODIS and ENVISAT's MERIS. Landsat sensors offer a high spatial resolution (30 m) but a fragmentary temporal coverage. The higher temporal resolution of MODIS and MERIS allow repeated global observations and offer the possibility to detect temporal changes and access seasonality. On the downside, the spatial resolution of these sensors is comparably low with 250 and 300 m, respectively.

GlobCover 2009

Based on ENVISAT's Medium Resolution Imaging Spectrometer (MERIS), 300 m resolution, a consortium led by ESA generated global land cover maps (GlobCover) for the years 2005/2006 (V2.2) and 2009 (V2.3). The automated and regionally adjusted classification distinguished 22 land cover classes according to the UN Land Cover Classification System (LCCS). The water mask is a by-product of the land cover classification process.

Access via: http://due.esrin.esa.int/page_globcover.php

MODIS 250m water mask (MOD44W) (2009)

The MODIS 250m land-water mask (MOD44W, Carroll et al. 2009) is the last member of a set of water masks. Predecessors were the EOS DEM-based land-water mask (Logan et al., 1999) and the MODIS Nadir Bidirectional Reflectance Distribution Function (BRDF)-Adjusted Reflectance (NBAR) and MODIS land cover-based global land-water mask (Salomon et al., 2004). The MODIS 250 m mask was produced from three different data sets:

1. The MOD44C, a non-public, 250 m global 16-day composite collection based on 8+ years of Terra MODIS data, and 6+ years of Aqua MODIS data.
3. The MODIS–based Mosaic of Antarctica (MOA) for areas between 60° S and 90° S.
1. The Shuttle Radar Topography Mission's (SRTM) Water Body Dataset (SWBD) restricted to areas between 60° S to 60° N.

The production was further supplemented by other publicly available data sets. The MODIS 250m water mask is provided in a special gridded tile structure that is common to higher-level MODIS land products. Reprojection can be performed via the MODIS Reprojection Tool (MRT).

Access: https://lpdaac.usgs.gov/products/mod44wv006/

Global Surface Water (2016)

The Global Surface Water tool is an interactive mapping tool of past surface water based on the Landsat 5, 7, and 8 time series. Within the framework of the Copernicus Programme run by the European Commission's Joint Research Centre, Pekel et al. (2016) developed an online tool to map location and temporal distribution of water bodies over 32 years from March 1984 to October 2015. The data basis is a statistical analysis of water extent from individual images from the Landsat 5 (TM), 7 (ETM+), and 8 (OLI) time series. The algorithm to detect water bodies is a combination of expert systems and evidential reasoning and uses the Normalized Difference Vegetation Index and a Hue-Saturation-Value (HSV) colour-space transformation to detect water bodies.

The website (https://global-surface-water.appspot.com/) provides free access to six datasets: occurrence, occurrence change intensity, seasonality, recurrence, transitions and maximum water extent. For all locations, statistics on the extent and change of water surface are provided.

ESA Climate Change Initiative (CCI) Water bodies v4.0 (2017)

The ESA Climate Change Initiative (CCI) provides a global land cover maps at 300 m spatial resolution, on an annual basis from 1992 to 2015. Also provided is a static map of open water bodies at an original spatial resolution of 150 m that was resampled to 300 m for the land cover classification. Water bodies result from a combination of SAR (Envisat ASAR water body indicator) and optical water body detection (Global Forest Change 2000 - 2012 and the Global Inland Water product) as well as auxiliary datasets. A detailed overview of the procedure gives Lamarche et al. (2017). The data is available via http://maps.elie.ucl.ac.be/CCI/viewer/.

9.1.4 Comparison of water masks

Detail sections of the study area compare the surface water extent deduced from nine published datasets and the here presented water body extraction approach (Figure 20 and Figure 21).

Stream networks developed from a) topographic maps and b) digital elevation models and are generally available as vectors. The **VMap 0** is globally the most comprehensive source of stream network information on a vector basis. On the downside, the stream network is not contiguous (i.d. showing gaps between tributaries) and the inland water areas by far overestimate the extent of surface water in the study area (cf. Figure 20). **HydroSHEDS** displays a network of **drainage pathways** derived from the SRTM digital elevation model. As a hypothetic stream network, it is not valid for most analyses interested in the actual presence or absence of surface water. Manually corrected and attributed, the **Global Lakes and Wetlands database** provides additional, ecological information for the classification of wetlands. On the downside, the stream network is restricted to major rivers and the coarse spatial resolution does not allow its use on a local scale.

Actual information on the presence or absence of water is only available from **remote sensing**. The approaches differ regarding the sensor/satellite, the water extraction algorithm, and the evaluated period. Static water masks such as **Envisat MERIS Global Land Cover Map 2009** (GlobCover 2009, 300 m), the **MODIS static water mask** (MOD44W, 250 m, Carroll et al. 2009) or the **ESA Climate Change Initiative** (150 m, Lamarche et al. 2017) show a snapshot of the surface water distribution during the respective year/time period. Information about variability is only available from time series analyses—now possible for Landsat and MODIS.

Envisat MERIS Global Land Cover Map 2009 (GlobCover 2009, 300 m) and the **MODIS static water mask** (**MOD44W**, 250 m) both use optical sensors and show comparable areas of surface water due to a similar spatial resolution. The **ESA Climate Change Initiative** (Lamarche et al. 2017) published a static water mask with a resolution of 150 m. It is based on the compilation of different sources including both SAR and optical sensors. Its permanent water bodies are in good agreement with the results of the Global Surface Water and strongly improve the static MODIS water mask (MOD44W, 250 m). The spatial resolution, however, is still very coarse with respect to small and seasonal water bodies as seen in the Dallol Maouri (Figure 20).

The approach presented in this study extracted water bodies from Landsat time series (spatial resolution of 30 m) using the MNDWI. It provides raster information on annual and monthly probability of flooding (water recurrence) and seasonality. The **Global Surface Water** project (Pekel et al. 2016) used the Landsat archive to compute similar indices of water recurrence and seasonality. Compared with the spectral index MNDWI, the more sophisticated approach of Pekel et al. (2016) shows a higher discriminatory power between water and land as shown for a water recurrence < 10 % (Figure 21). Our approach using the MNDWI shows a higher flooding variability as expressed by the large water recurrence classes 10 % - 80 %. Whereas the Global Surface Water suggests a larger extent of reliable flooded areas (> 80 % of observed scenes) compared to the MNDWI, the extent of variably flooded areas (< 80 %) delimited by the MNDWI considerably exceeds the areas designated as variable by the Global Surface Water project. Compared with the Global Surface Water, our approach is more conservative regarding the reliably flooded areas but likely overestimates the areas of variable flooding.

Table 7: Selection of public available stream networks and water body datasets.

Dataset	Source Data	Year	Reference	Resolution	Coverage	(Dis-) Advantage	Comment	Access & Dokumentation
VMap0 Vector Smart Map (level 0)	Digital Chart of the World & Operational	1992	National Imagery and Mapping Agency's (NIMA)	1:1.000.000 VMap1 & Vmap2 are higher resolution national data	global	+ comprehensive + often only available dataset - low resolution -		Mapability: http://www.mapability.com/index1.html GISLab: http://gis-lab.info/qa/vmap0-eng.html
HYDRO1K	GOTOPO30 (1996)	1996	USGS	30 arc seconds (approx.. 1 km)	global	- low resolution (1km) - outdated		http://earthexplorer.usgs.gov/ https://lta.cr.usgs.gov/HYDRO1KReadMe
SWBD Shuttle Radar Topography Mission (SRTM)	SRTM DEM DTED2 (1 arc-second)	2003 ?	USGS	Vector format Dimensions differ between lakes, rivers, and shoreline	56° South to 60° North	- only water areas >600m - no rivers - Stand: 2000 (SRTM Mission)		http://earthexplorer.usgs.gov/
GLWD Global Lakes and Wetlands Database	Maps and others	2004	(Lehner und Döll 2004)	Maps: 1:1 – 3 Mio Lakes >0.1 km² Raster data: 30 arcsec (approx.. 1 km)	global 1.4 Mio global lakes (>10ha)	+ comprehensive + Metadata - low resolution (1 km)	Recompilation from a variety of sources	http://www.worldwildlife.org/pages/global-lakes-and-wetlands-database
HydroSHEDS & HydroLAKES	SRTM DTED1 (3 arc second)	2008	(Lehner, Verdin & Jarvis 2008)	3 arc-seconds (approx.. 90 m) to 30 arc-seconds (approx.. 1 km)	56° South to 84° North	+ comprehensive even in remote areas + medium resolution (15 sec) - potential drainage only - Stand: 2000 (SRTM Mission)	Based on by GLWD, DCW, SWDB, SRTM DEM various models	http://www.hydrosheds.org/
GlobCover Global land cover map	Envisat/MERIS	2009	ESA	300m	global	+ direct water detection - single year only - low resolution	GlobCover, Water as a by-product	http://due.esrin.esa.int/page_globcover.php
MOD44W MODIS 250m Water Mask	MODIS 16 day composite	2009	(Carroll et al. 2009)	250m	Sinusoidal projection	+ direct water detection - low spatial resolution	MODIS Terra & Aqua 16 day composite SWDB (2003)	https://search.earthdata.nasa.gov/ https://lpdaac.usgs.gov/dataset_discovery/modis/modis_products_table/mod44w
Global Surface Water	Landsat time series	1984-2015	Pekel et al. (2016)	30m	global	+ direct water detection + high spatial resolution + time series 1984 – 2015 + freely available	Conservative and robust approach	https://global-surface-water.appspot.com/
ESA CCI Water bodies v4.0	Compilation of SAR & optical sensors	2000-2012	Lamarche et al., (2017)	150m	global	+ comprehensive. robust and compatible with ESA Land Cover time series - average spatial resolution	static average water surface map of the years 200-2012	http://maps.elie.ucl.ac.be/CCI/viewer/ http://maps.elie.ucl.ac.be/CCI/viewer/download.php
Benin-Niger-Nigeria	Landsat time series	1984-2016	this study, 2017	30m	transboundary study area Benin-Niger-Nigeria	+ direct water detection (MNDWI) + high spatial resolution + time series 1984 – 2015	Modified Normalized Difference Water Index (MNDWI) is more sensitive than the conservative approach by Pekel et al. (2016)	this study

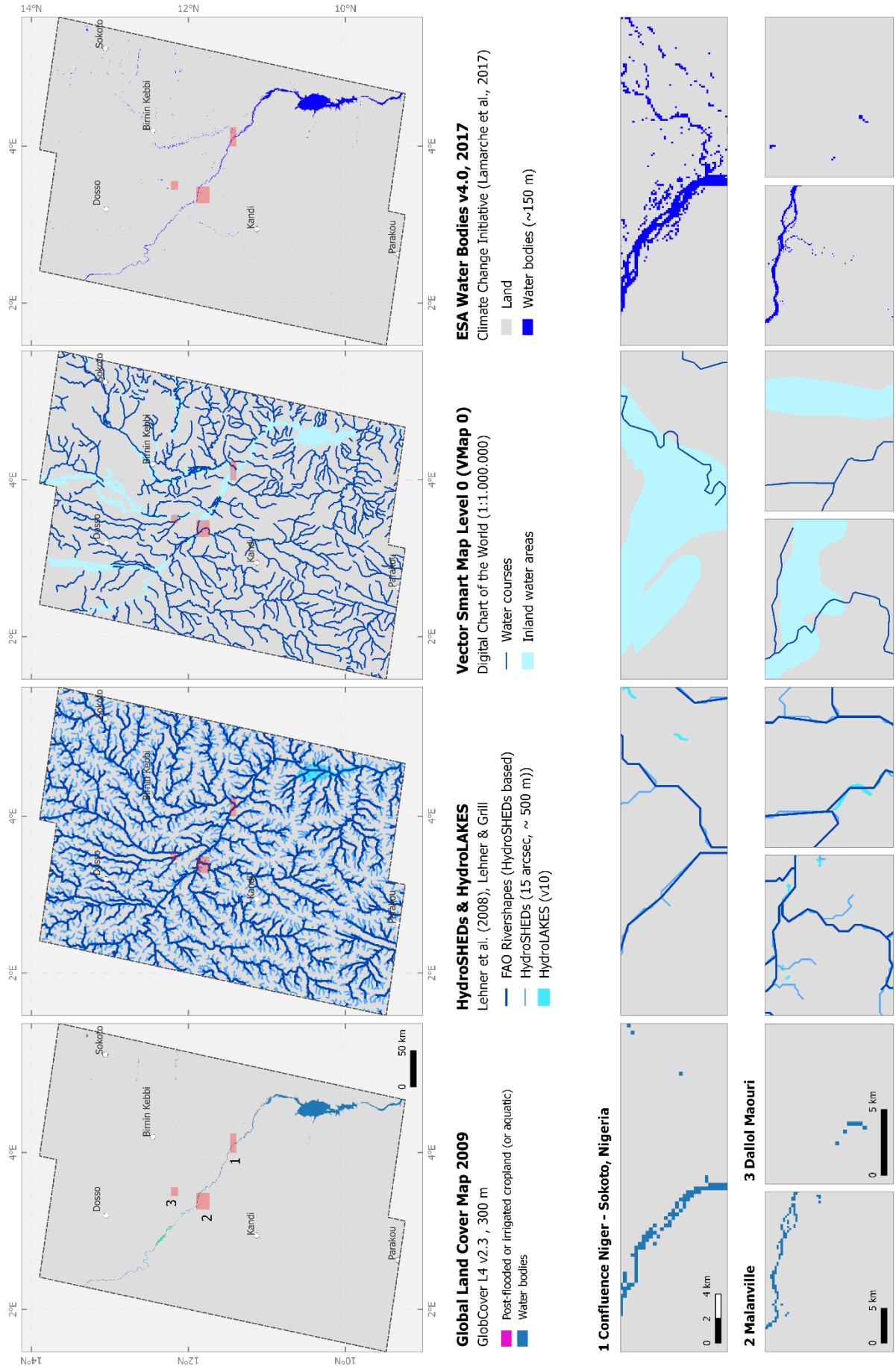

Figure 20: Comparison of water masks and stream networks I

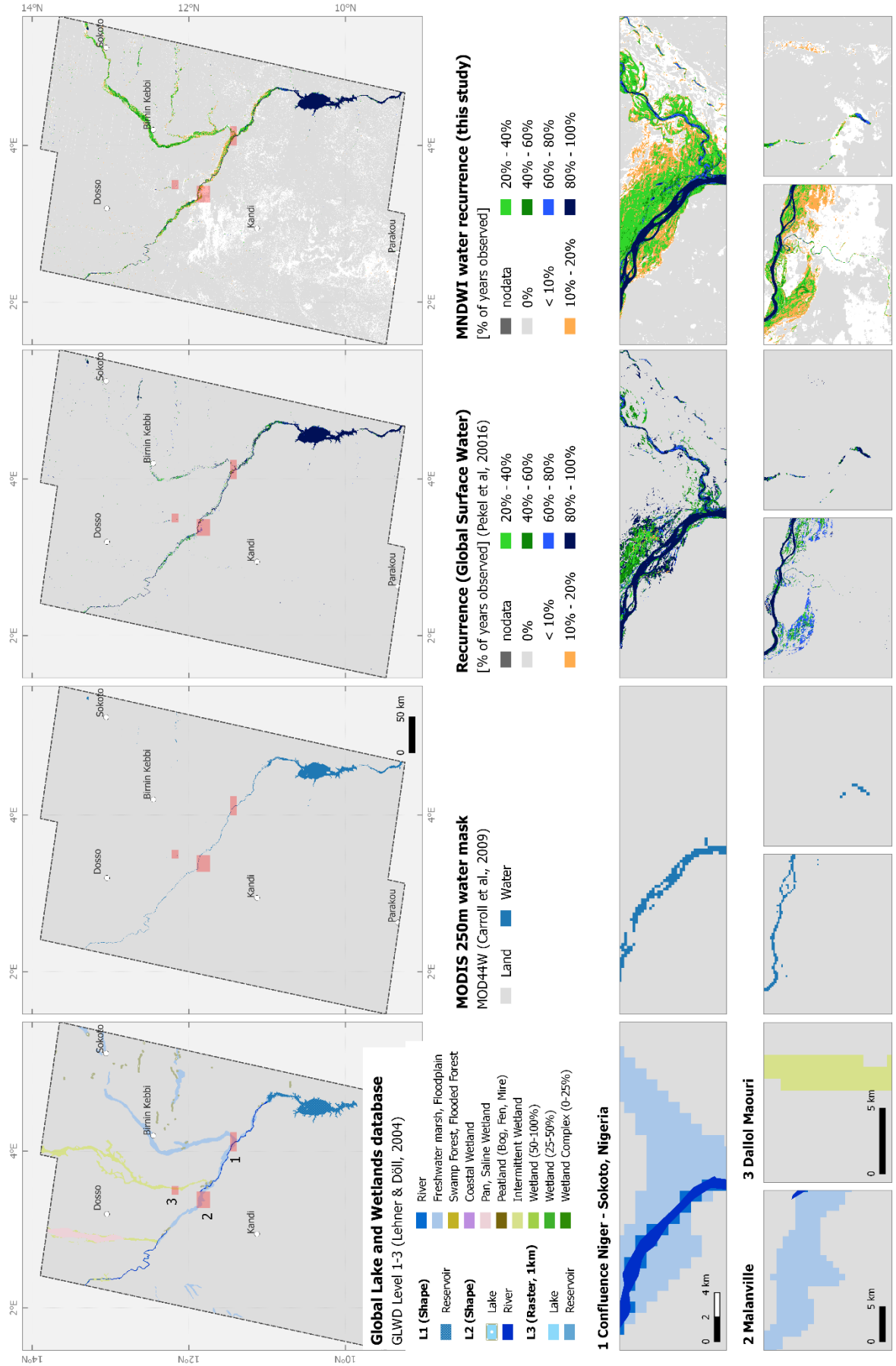

Figure 20 cont.: Comparison of water masks and stream networks II

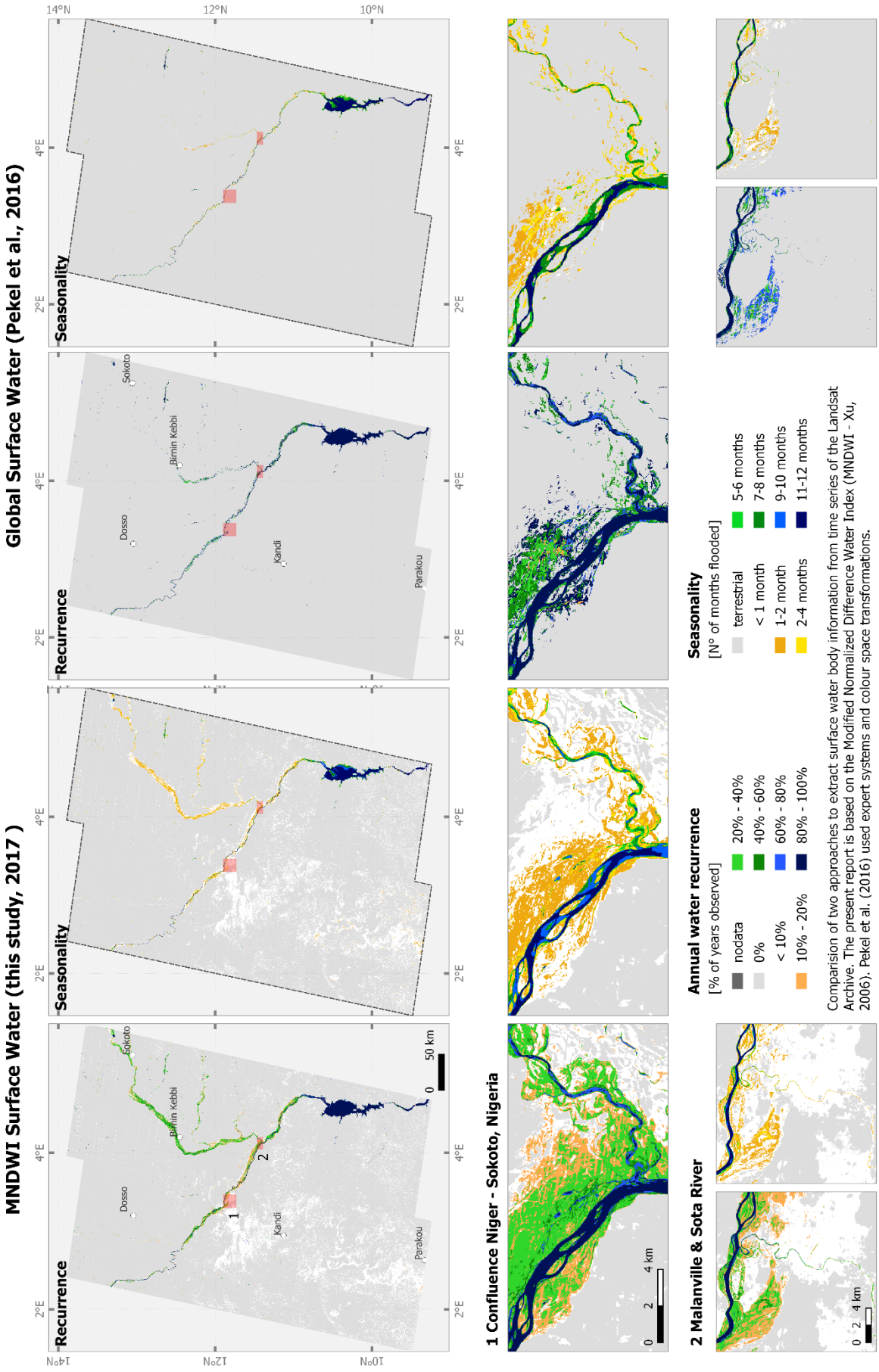

Figure 21. Comparison of water recurrence (probability of flooding) and seasonality calculated by Pekel et al. (2016) on a combination of NDVI, expert systems, and hue values and in this study using the MNDWI.

9.2 Technical implementation: QGIS & Python

9.2.1 Technical Requirements

Automated processing of Landsat scenes requires extensive amounts of disk space and processing power. Whereas *numpy* calculation can be conducted in the memory, the QGIS raster calculator writes intermediate results to the disk. For the six Landsat tiles, a minimum of about 600 GB of free disk space is necessary.

Scripting of python and integration of QGIS algorithms within the python interface requires a sound knowledge of both python and QGIS programming.

At the time of processing, QGIS raster calculator was not able to handle raster layers with different spatial extents due to the occurrence of not defined values. Instead, the python package *numpy* was used, which, on the other hand, was limited to calculations within a local coordinate system.

9.2.2 Python script

The outlined procedures were translated into a *Python 2.7* script and run within the modelling environment of *QGIS 2.14.9 Essen*. The python script works on a tile basis. For each tile, between 261 and 326 single Landsat scenes were available. For each scene, the spectral index was calculated. Clouds, snow and cloud shadows were masked using the provided CFmask. Raster calculations were performed on single scenes with a common spatial extent using the python package *numpy*.

In a second step, summary statistics for the respective tile were calculated across sensors. Being of different spatial extent, raster calculations within a geographic coordinate system require the use of the raster calculator implemented in QGIS.

9.2.3 Input Data & Folder Structure

Input data are Landsat 4, 5, 7, and 8 Pre-Collection Surface Reflectance Data. Each scene is stored in a single folder (Figure 22).

Input Folder: The input folder must strictly adhere to the following rules. Landsat tiles are arranged following Sensors (obligate folder names are: Landsat_4-5_TM, Landsat_7_ETMP, Landsat_8_OLI), Tiles (obligate folder names must include Landsat sensor in addition to the tile (e.g. L7_192_052) and finally the single Landsat scenes each in its own folder.

Output folder: Output folders differentiate between single scene calculations processed with numpy and summary results calculated with QGIS. Single scene intermediate results are stored in the “\outputs” folder. Summary results over the entire Landsat Archive are stored in the “\results” folder.

Sensors: The sensors (TM, ETM+, and OLI) to be included have to be specified explicitly within the input parameter section of the program. This information is crucial as band assignations and parameters vary according to the type of sensor

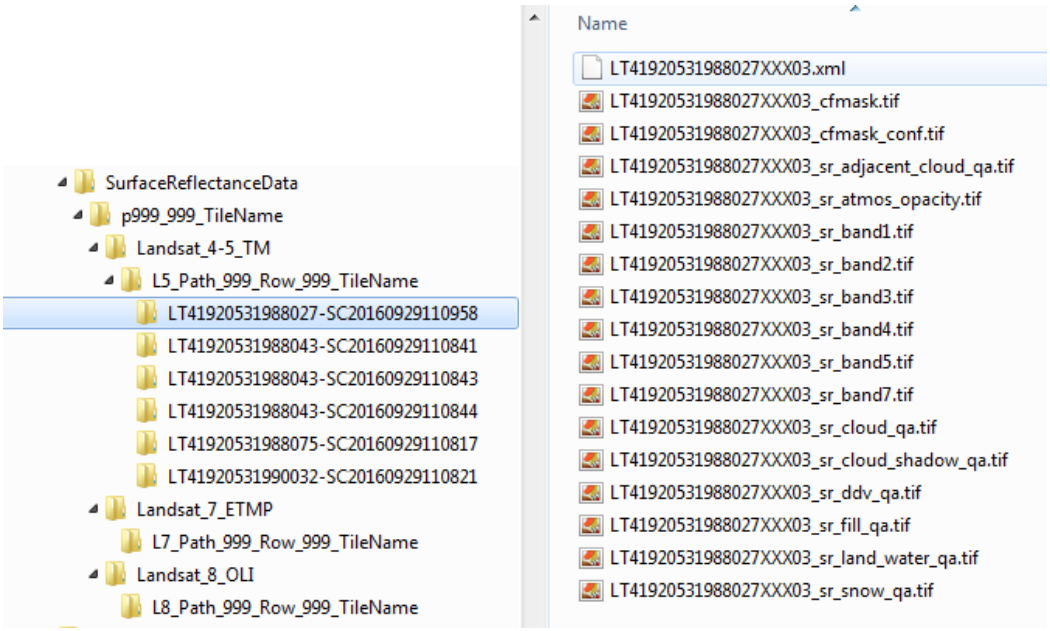

Figure 22: Proposed folder structure for the python program

9.2.4 Digital datasets

A dataset with the annual and monthly probability of flooding, seasonality and the openly available stream network data is collated in the accompanying QGIS project.

9.3 Figures

Table 8: Surface Reflectance Specifications for Landsat 7 ETM+ data. (Pre-Collection, from USGS 2016a).

INT16 16-bit signed integer, UINT8 8-bit unsigned integer, QA quality assurance, DDV dark dense vegetation, CFMask C version of Function of Mask, NA not applicable

Band Designation	Band Name	Data Type	Units	Range	Valid Range	Fill Value	Saturate Value	Scale Factor
sceneid_sr_band1	Band 1	INT16	Reflectance	-2000 – 16000	0 - 10000	-9999	20000	0.0001
sceneid_sr_band2	Band 2	INT16	Reflectance	-2000 – 16000	0 - 10000	-9999	20000	0.0001
sceneid_sr_band3	Band 3	INT16	Reflectance	-2000 – 16000	0 - 10000	-9999	20000	0.0001
sceneid_sr_band4	Band 4	INT16	Reflectance	-2000 – 16000	0 - 10000	-9999	20000	0.0001
sceneid_sr_band5	Band 5	INT16	Reflectance	-2000 – 16000	0 - 10000	-9999	20000	0.0001
sceneid_sr_band7	Band 7	INT16	Reflectance	-2000 – 16000	0 - 10000	-9999	20000	0.0001
sceneid_sr_atmos_opacity[1]	Atmospheric Opacity	INT16	Unitless	-2000 – 16000	0 - 10000	-9999	NA	0.0010
sceneid_sr_fill_qa	Fill QA	UINT8	Value Flag	0 not fill 255 fill	0 not fill 255 fill	NA	NA	NA
sceneid_sr_ddv_qa	DDV QA	UINT8	Value Flag	0 not DDV 255 DDV	0 not DDV 255 DDV	NA	NA	NA
sceneid_sr_cloud_qa	Cloud QA	UINT8	Value Flag	0 not cloud 255 cloud	0 not cloud 255 cloud	NA	NA	NA
sceneid_sr_cloud_shadow_qa	Cloud Shadow QA	UINT8	Value Flag	0 not cloud shadow 255 cloud shadow	0 not cloud shadow 255 cloud shadow	NA	NA	NA
sceneid_sr_snow_qa	Snow QA	UINT8	Value Flag	0 not snow 255 snow	0 not snow 255 snow	NA	NA	NA
sceneid_sr_land_water_qa	Land Water QA	UINT8	Value Flag	0 land 255 water	0 land 255 water	NA	NA	NA
sceneid_sr_adjacent_cloud_qa	Adjacent Cloud QA	UINT8	Value Flag	0 not adjacent cloud 255 adjacent cloud	0 not adjacent cloud 255 adjacent cloud	NA	NA	NA
sceneid_sr_cfmask	CFMask	UINT8	Value Flag	0 clear 1 water 2 cloud shadow 3 snow 4 cloud	0 clear 1 water 2 cloud shadow 3 snow 4 cloud	255	NA	NA
sceneid_sr_cfmask_conf	CFMask Cloud Confidence	UINT8	Value Flag	0 none 1 low confidence 2 medium confidence 3 high confidence	0 none 1 low confidence 2 medium confidence 3 high confidence	255	NA	NA

1 General interpretation for atmospheric opacity: < 0.1 = clear; 0.1 – 0.3 = average; > 0.3 = hazy.

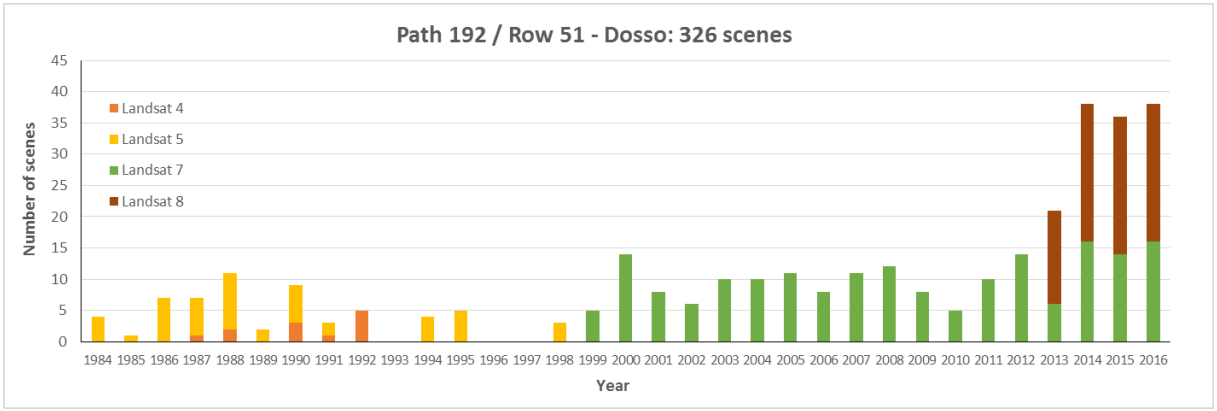

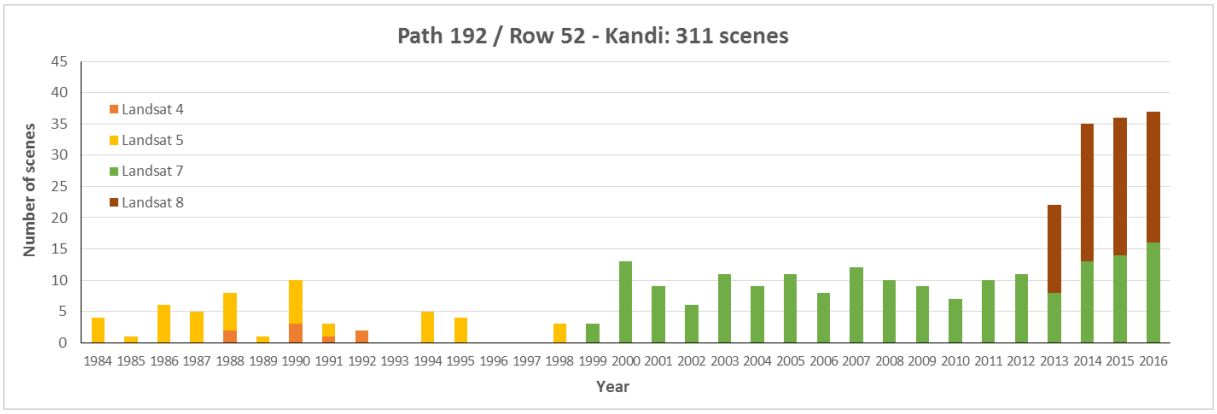

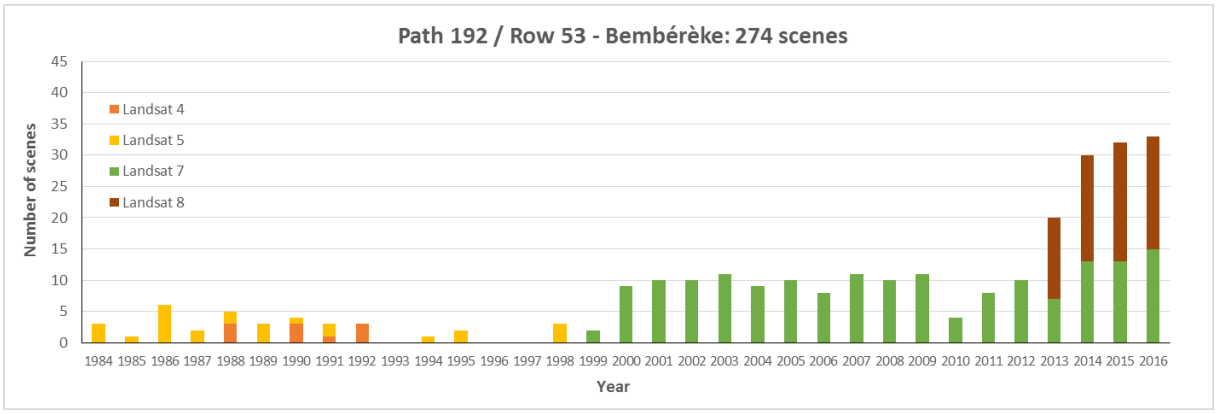

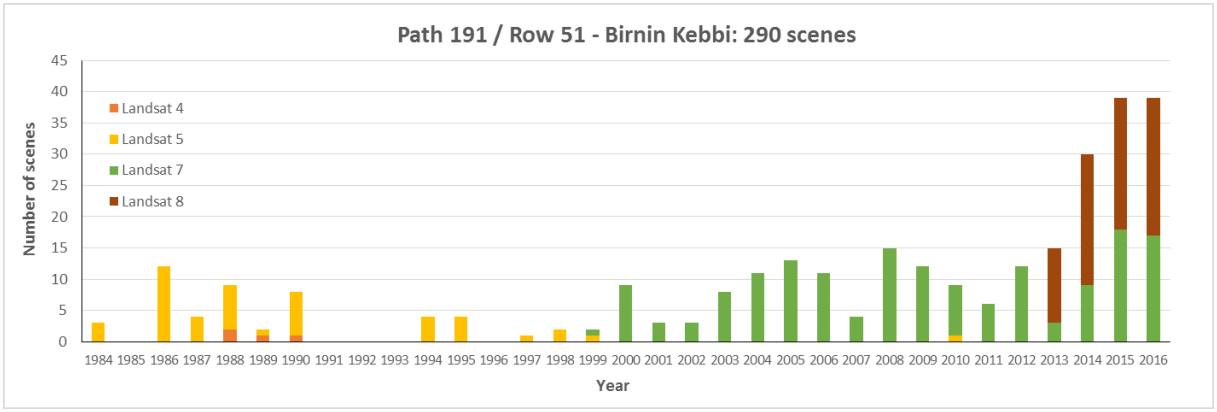

Figure 23: Sensor type and number of available scenes between 1984 and 2016

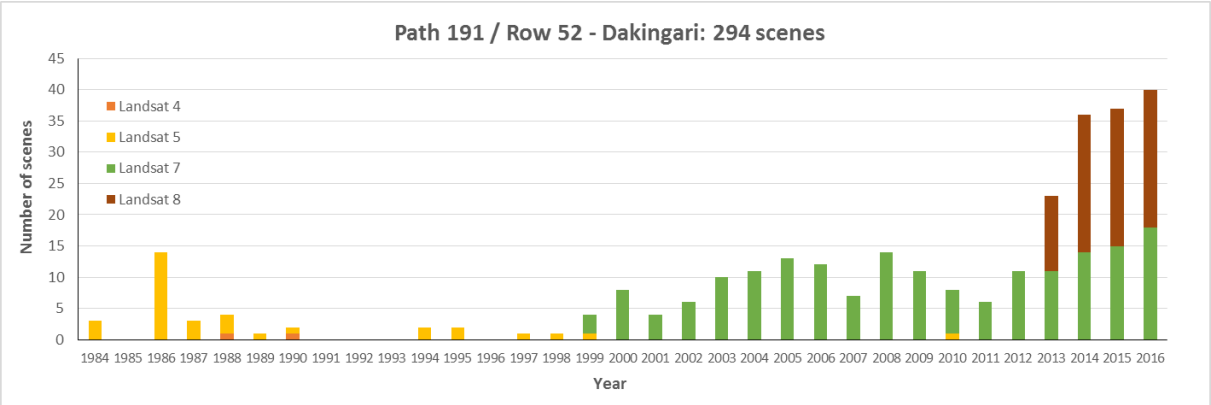

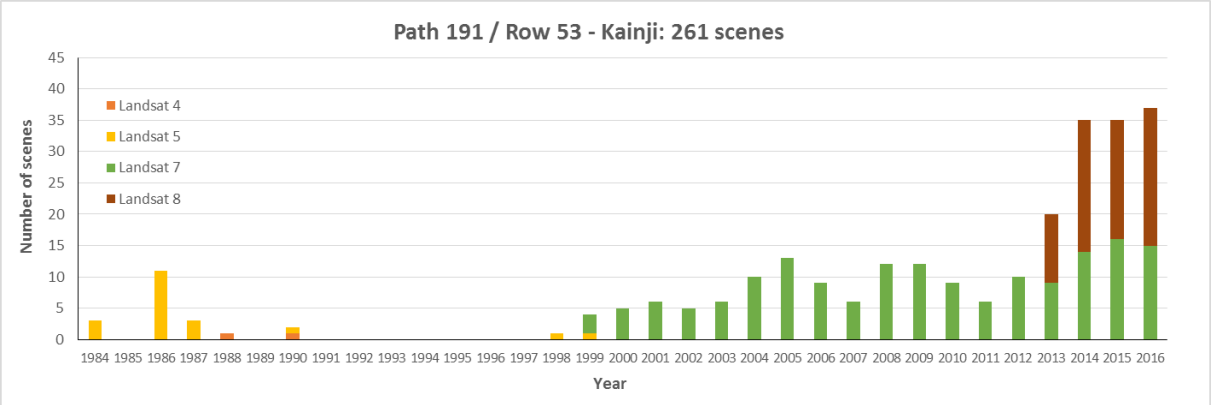

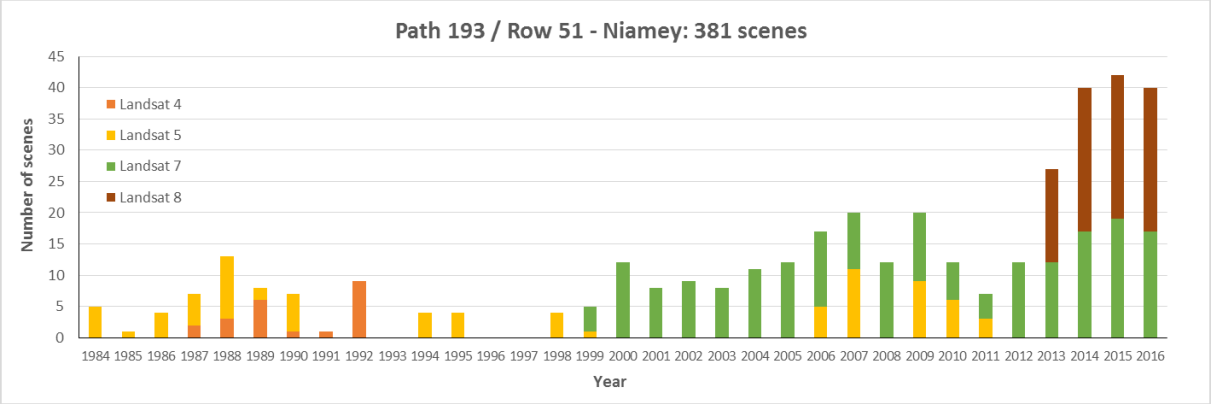

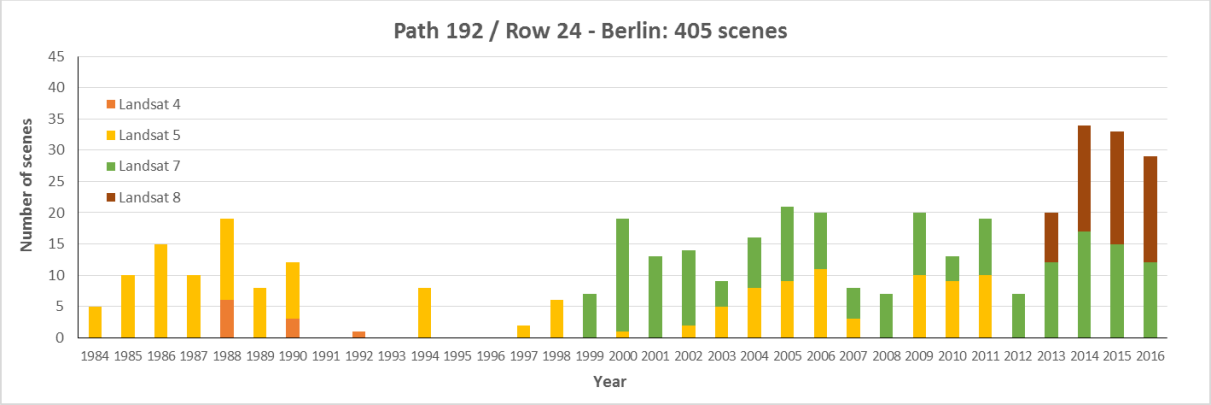

Figure 23: continued

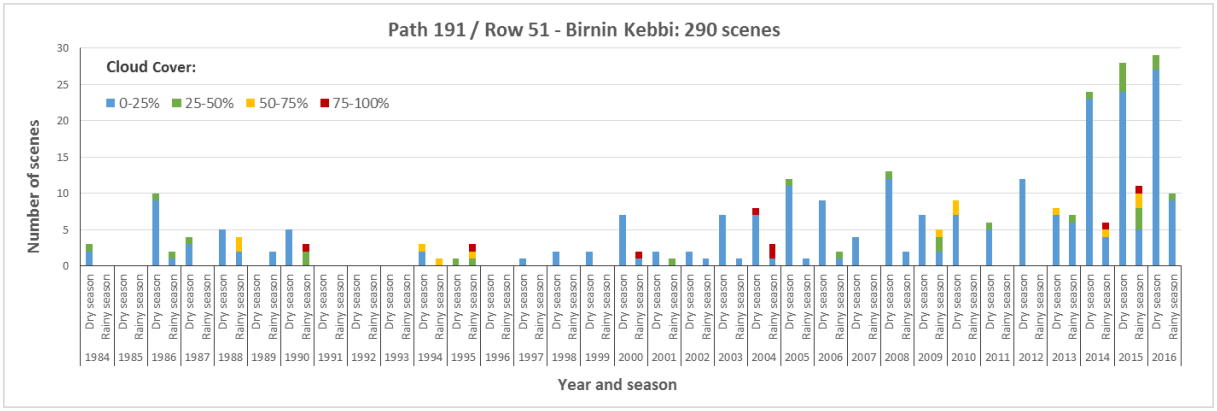

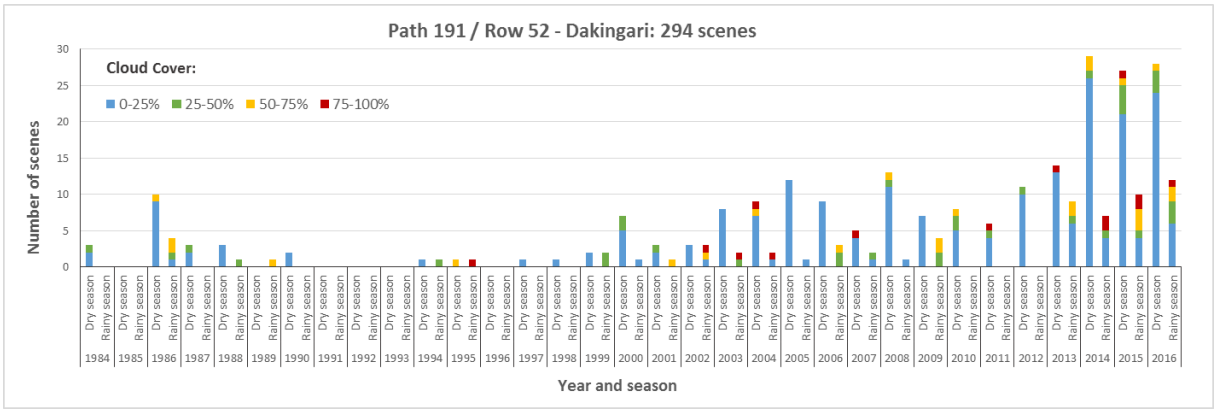

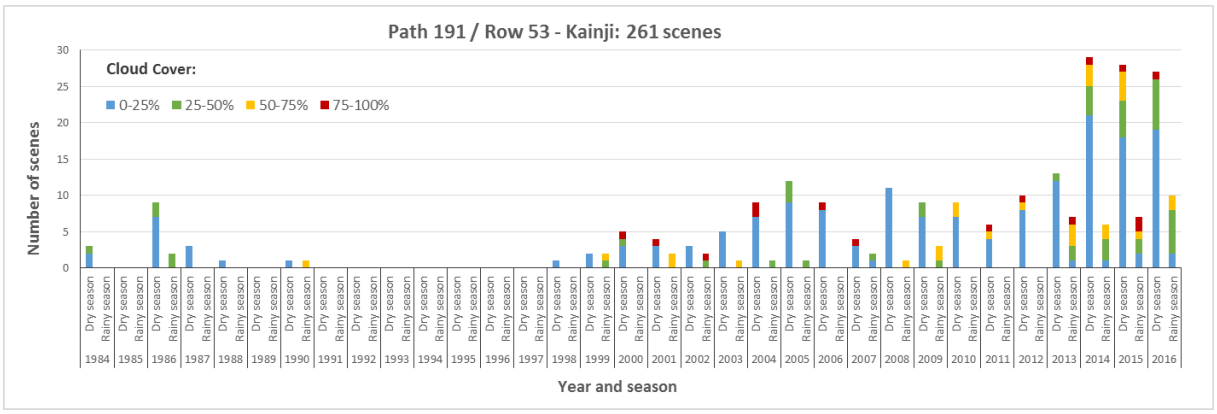

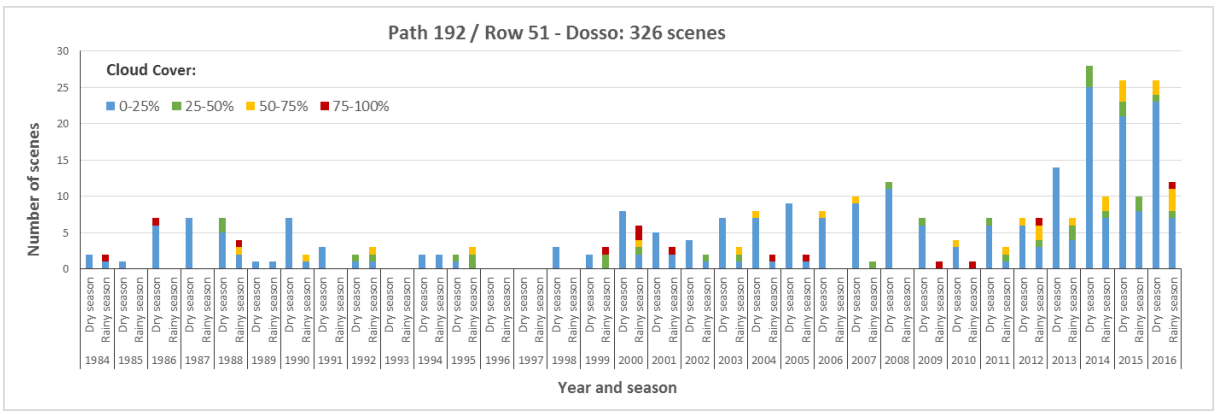

Figure 24: Seasonal distribution and cloud cover for available satellite scenes.

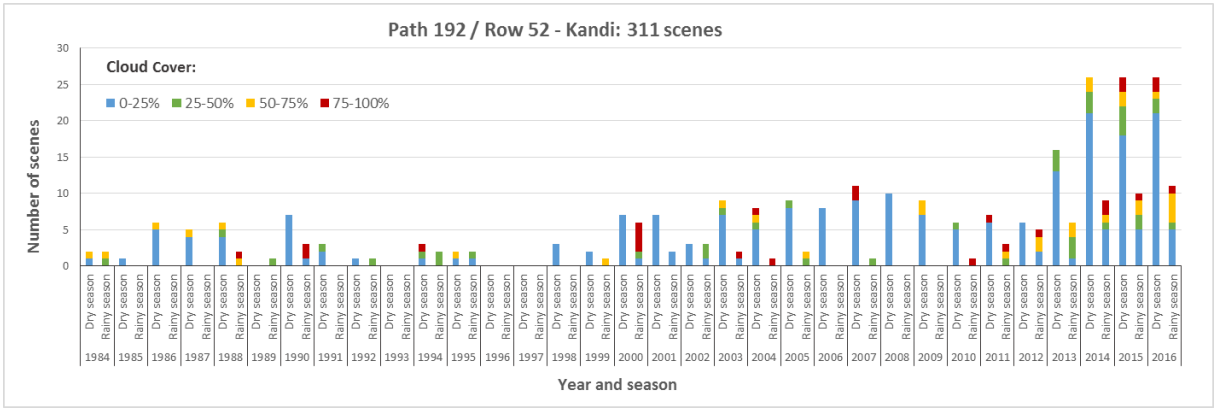

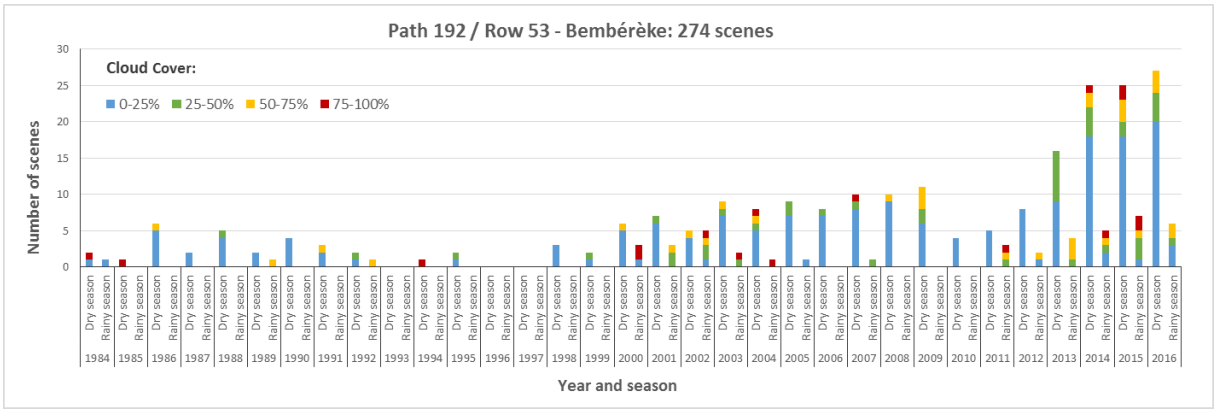

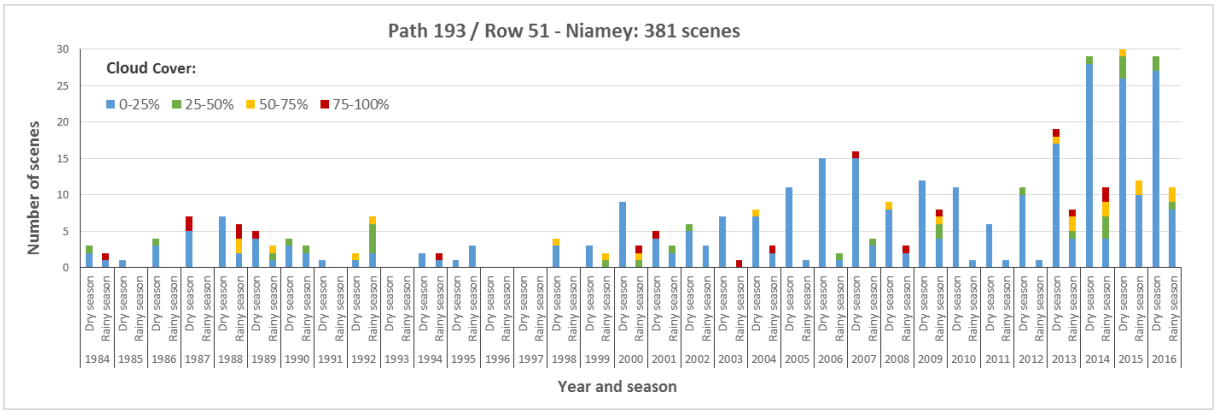

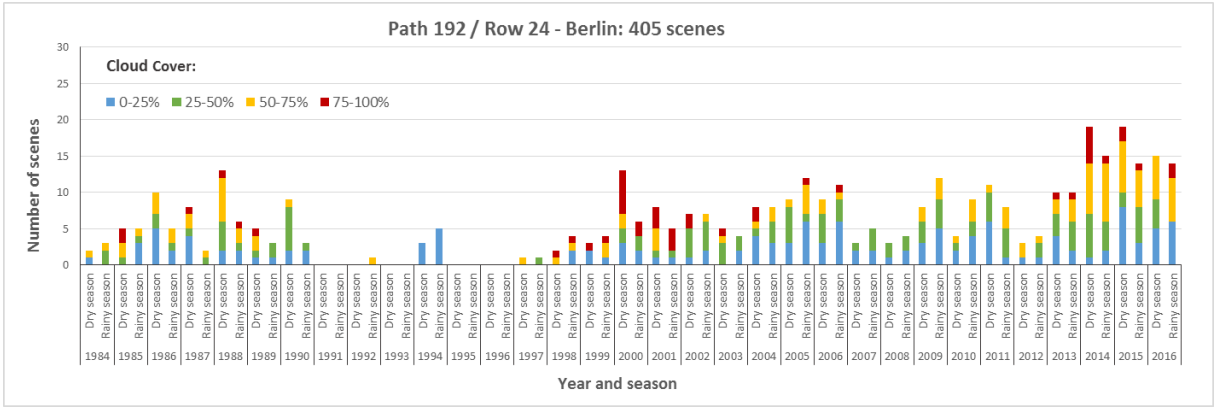

Figure 24: continued